

1 Non-Hydrostatic RegCM4 (RegCM4-NH): Model description and
2 case studies over multiple domains.

3 Erika Coppola (1), Paolo Stocchi (2), Emanuela Pichelli (1), Jose Abraham Torres Alavez
4 (1), Russel Glazer (1), Graziano Giuliani (1), Fabio Di Sante (1), Rita Nogherotto (1),
5 Filippo Giorgi (1)

6
7 *Correspondence to:* Erika Coppola (coppolae@ictp.it)

8 1. International Centre for Theoretical Physics (ICTP), Trieste, Italy

9 2. Institute of Atmospheric Sciences and Climate, National Research Council of Italy,
10 CNR-ISAC, Bologna, Italy

11 **Abstract.** We describe the development of a non-hydrostatic version of the regional
12 climate model RegCM4, called RegCM4-NH, for use at convection-permitting resolutions.
13 The non-hydrostatic dynamical core of the Mesoscale Model MM5 is introduced in the
14 RegCM4, with some modifications to increase stability and applicability of the model to
15 long-term climate simulations. Newly available explicit microphysics schemes are also
16 described, and three case studies of intense convection events are carried out in order to
17 illustrate the performance of the model. They are all run at convection-permitting grid
18 spacing of 3 km over domains in northern California, Texas and the Lake Victoria region,
19 without the use of parameterized cumulus convection. A substantial improvement is found
20 in several aspects of the simulations compared to corresponding coarser resolution (12
21 km) runs completed with the hydrostatic version of the model employing parameterized
22 convection. RegCM4-NH is currently being used in different projects for regional climate
23 simulations at convection-permitting resolutions, and is intended to be a resource for
24 users of the RegCM modeling system.

25

26 **Keywords**

27 Regional climate models; RegCM4; km-scale resolution; climate change

28 **Introduction**

29 Since the pioneering work of Dickinson et al. (1989) and Giorgi and Bates (1989),
30 documenting the first regional climate modeling system (RegCM, version 1) in literature,
31 the dynamical downscaling technique based on limited area Regional Climate Models
32 (RCMs) has been widely used worldwide, and a number of RCM systems have been
33 developed (Giorgi 2019). RegCM1 (Dickinson et al., 1989, Giorgi and Bates, 1989) was
34 originally developed at the National Center for Atmospheric Research (NCAR) based on
35 the Mesoscale Model version 4 (MM4) (Anthes et al, 1987) . Then, further model versions
36 followed: RegCM2 (Giorgi et al. 1993a,b), RegCM2.5, (Giorgi and Mearns 1999),
37 RegCM3 (Pal et al. 2007), and lastly RegCM4 (Giorgi et al 2012). Except for the transition
38 from RegCM1 to RegCM2, in which the model dynamical core was updated from that of
39 the MM4 to that of the MM5 (Grell et al. 1994), these model evolutions were mostly based
40 on additions of new and more advanced physics packages. RegCM4 is today used by a
41 large community for numerous projects and applications, from process studies to paleo
42 and future climate projections, including participation in the Coordinated Regional
43 Downscaling EXperiment (CORDEX, Giorgi et al. 2009; Gutowski et al. 2016). The model
44 can also be coupled with ocean, land and chemistry/aerosol modules in a fully interactive
45 way (Sitz et al. 2017).

46 The dynamical core of the standard version of RegCM4 is hydrostatic, with sigma-p
47 vertical coordinates. As a result, the model can be effectively run for grid spacings of ~10
48 km or larger, for which the hydrostatic assumption is valid. However, the RCM community
49 is rapidly moving to higher resolutions of a few km, i.e. “convection-permitting” (Prein et
50 al. 2015; Coppola et al. 2020) and therefore the dynamical core of RegCM4 has been
51 upgraded to include a non-hydrostatic dynamics representation usable for very high
52 resolution applications. This upgrade, which we name RegCM4-NH, is essentially based
53 on the implementation of the MM5 non-hydrostatic dynamical core within the RegCM4
54 framework, which has an entirely different set of sub-grid model physics compared to
55 MM5.

56

57 RegCM4-NH is already being used in some international projects focusing on climate
58 simulations at convection-permitting km-scales, namely the European Climate Prediction

59 System (EUCP, Hewitt and Lowe 2018) and the CORDEX Flagship Pilot Study dedicated
60 to convection (CORDEX-FPSCONV, Coppola et al. 2020), and it is starting to be used
61 more broadly by the RegCM modeling community.

62 For example, the recent papers by Ban et al. (2021) and Pichelli et al. (2021) document
63 results of the first multi-model experiment of 10-year simulations at the convection-
64 permitting scales over the so-called greater Alpine region. Two different simulations with
65 RegCM4-NH for present day conditions have contributed to the evaluation analysis of
66 Ban et al. (2021). They were carried out at the International Centre for Theoretical Physics
67 (ICTP) and the Croatian Meteorological and Hydrological Service (DHMZ) using two
68 different physics configurations. The results show that RegCM4-NH largely improves the
69 precipitation simulation as compared to available fine scale observations when going from
70 coarse to high resolution, in particular for higher order statistics, such as precipitation
71 extremes and hourly intensity. Pichelli et al. (2021) then analyse multi-model ensemble
72 simulations driven by selected CMIP5 GCM projections for the decades 1996–2005 and
73 2090–2099 under the RCP8.5 scenario. ICTP contributed to the experiment with
74 simulations using RegCM4-NH driven by the MOCH-HadGEM GCM (r1i1p1) in a two
75 level nest configuration (respectively at 12 and 3 km grid). The paper shows new insights
76 into future changes, for example an enhancement of summer and autumn hourly rainfall
77 intensification compared to coarser resolution model experiments, as well as an increase
78 of frequency and intensity of high-impact weather events.

79
80 In this paper we describe the structure of RegCM4-NH and provide some illustrative
81 examples of its performance, so that model users can have a basic reference providing
82 them with background information on the model. In the next section we first describe the
83 new model dynamical core, while the illustrative applications are presented in section 4.
84 Section 5 finally provides some discussion of future developments planned for the RegCM
85 system.

86

87 **Model description**

88 In the development of RegCM4-NH, the RegCM4 as described by Giorgi et al. (2012) was
89 modified to include, the non-hydrostatic dynamical core (*idynamic* = 2 namelist option as
90 described in RegCM-4.7.1/Doc/README.namelist of the source code) of the mesoscale
91 model MM5 (Grell et al. 1994). This dynamical core was selected because RegCM4
92 already has the same grid and variable structure as MM5 in its hydrostatic core, which
93 substantially facilitated its implementation (Elguindi et al. 2017).

94

95 The model equations with complete description of the Coriolis force and a top radiative
96 boundary condition, along with the finite differencing scheme, are given in Grell et al.
97 (1994). Pressure, p , temperature, T , and density, ρ , are first decomposed into a
98 prescribed reference vertical profile plus a time varying perturbation. The prognostic
99 equations are then calculated using the pressure perturbation values. Compared to the
100 original MM5 dynamical core, the following modifications were implemented in order to
101 achieve increased stability for long term climate simulations (Elguindi et al. 2017
102 document any modifications which follow the choice of the non-hydrostatic dynamical
103 core through the namelist parameter *idynamic* = 2; further available user-dependant
104 options, and the corresponding section in the namelist, are explicitly indicated):

105

106 i) The reference state temperature profile is computed using a latitude dependent
107 climatological temperature distribution and thus is a function of the specific domain
108 coordinates (*base_state_pressure*, *logp_lrate* parameters in *&referenceatm*) (Elguindi et
109 al. 2017). These two parameters were hard-coded in the original MM5 while for the
110 RegCM are user configurable;

111

112 ii) The lateral time dependent boundary conditions (*iboudy* in *&physicsparam*) for each
113 prognostic variable use the same exponential relaxation technique (*iboudy* = 5) described
114 in Giorgi et al. (1993). The linear MM5 relaxation scheme is also kept as an option (*iboudy*
115 = 1);

116

117 iii) The advection term in the model equations, which in the MM5 code is implemented
 118 using a centered finite difference approach, was changed to include a greater upstream
 119 weight factor as a function of the local Courant number (Elguindi et al. 2017). The
 120 maximum value of the weight factor is user configurable (*uoffc* in *&dynparam*). As detailed
 121 in the MM5 model description (Grell et al., 1994), the horizontal advection term for a scalar
 122 variable X contributes to the total tendency as:

123

$$\Delta_{adv}(p^*X)_G = -m^2|_G \left[\frac{(p^*X|_{b\frac{u}{m}}|_b - p^*X|_{a\frac{u}{m}}|_a)}{dx} + \frac{(p^*X|_{d\frac{v}{m}}|_d - p^*X|_{c\frac{v}{m}}|_c)}{dy} \right]$$

124

125

126 where the m is the projection mapping factor and, with respect to Figure 1, assuming that
 127 the computation is to be performed for the gold cross point G , the averages are performed
 128 in the points a, b, c, d . For the u/m and v/m terms, the average value is computed using
 129 respectively the values in points AC, BD, CD, AB .

130 In RegCM4 for the term p^*X , the model computes a weighted average value of the field
 131 using the value in gold+cyan and gold+green cross points with weights increasing the
 132 relative contribution of the upstream point up as a function of the local courant number:

133

$$134 \quad p^*X|_a = 0.5((1 - f_1)p^*X|_G + (1 + f_1)p^*X|_{c_1})$$

$$135 \quad p^*X|_b = 0.5((1 - f_1)p^*X|_{c_2} + (1 + f_1)p^*X|_G)$$

$$136 \quad p^*X|_c = 0.5((1 - f_2)p^*X|_G + (1 + f_2)p^*X|_{g_1})$$

$$137 \quad p^*X|_d = 0.5((1 - f_2)p^*X|_{g_2} + (1 + f_2)p^*X|_G)$$

138 where f_1, f_2 are defined as the local Courant number for the 1D advection equations
 139 multiplied for a control factor:

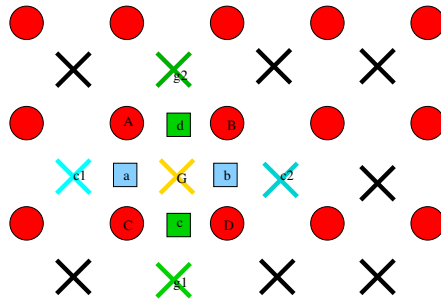
140

$$141 \quad f_1 = \mu_{fc}dt \frac{(u|_a + u|_b)}{2dx}$$

$$142 \quad f_2 = \mu_{fc}dt \frac{(v|_c + v|_d)}{2dy} ;$$

143

144



145

146 **Figure 1 Schematic representation showing the horizontal advection scheme**
 147 **staggering. Circles are U,V points. X are scalar variable points.**

148

149

150 iv) The water species (cloud, ice,rain, snow) term uses the same advection scheme as
 151 the other variables (Elguindi et al. 2017) and not a complete upstream scheme as in the
 152 MM5 code (Grell et al. 1994);

153

154 v) A local flux limiter reduces the advection terms in order to remove unrealistic strong
 155 gradients and its limits are user configurable (in the *&dynparam* section the maximum
 156 gradient fraction for advection: temperature, *t_extrema*, specific humidity, *q_rel_extrema*,
 157 liquid cloud content, *c_rel_extrema* and for tracers, *t_rel_extrema*). This was hardcoded
 158 in the MM5 code and the limits were not user configurable;

159

160 vi) The diffusion stencil of the Laplace equation uses a nine point approach as in LeVeque
 161 (2006) and a topography dependent environmental diffusion coefficient is added to
 162 reduce spurious diffusion along pressure coordinate slopes (Elguindi et al. 2017) as in
 163 the hydrostatic version of the code (Giorgi et al. 1993b). The change in stencil does not
 164 affect the overall fourth order precision of the model, but reduces the computational
 165 stencil size, thus reducing the communication overhead;

166

167 vii) The top boundary radiative condition (*ifupr = 1* in *&nonhydroparam*) adopted in the
 168 semi-implicit vertical differencing scheme to reduce the reflection of energy waves uses
 169 coefficients on a 13x13 matrix which are re-computed every simulation day and not kept
 170 constant throughout the whole simulation as in the MM5 code. This allows the model to

171 be run for longer simulation times while not being strongly tied to the initial atmospheric
 172 conditions;

173
 174 viii) The dynamical control parameter β in the semi-implicit vertical differencing scheme
 175 (*nhbet* in *&nonhydroparam*) used for acoustic wave damping (Elguindi et al. 2017) is user
 176 configurable (Klemp and Dudhia, 2008), while it is hard-coded in the MM5;

177
 178 ix) A Rayleigh damping (*ifrayd* = 1 in *&nonhydroparam*) of the status variables towards
 179 the input GCM boundary conditions can be activated in the top layers (*rayndamp*
 180 configuring the number of top levels to apply) with a configurable relaxation time
 181 (*rayalpha0*, Klemp and Lilly, 1978, Durran and Klemp, 1983. This is consistent to what is
 182 implemented in the WRF model);

183
 184 x) The water species time filtering uses the Williams (2009) modified filter with $\alpha = 0.53$
 185 instead of the RA filter used by all the other variables. The v factor in the RA filter is user
 186 configurable (*gnu1* and *gnu2* in *&dynparam*). This reduces the damping introduced by the
 187 Robert-Asselin filter and the computational diffusion introduced by the horizontal
 188 advection scheme.

189
 190 With these modifications, the model basic equations, under leap-frog integration scheme,
 191 are (Elguindi et al. 2017) :

192
 193

$$\frac{\partial p^* u}{\partial t} = -m^2 \left[\frac{\partial p^* uu/m}{\partial x} + \frac{\partial p^* vu/m}{\partial y} \right] - \frac{\partial p^* u \dot{\sigma}}{\partial \sigma} + uDIV - \frac{mp^*}{\rho} \left[\frac{\partial p'}{\partial x} - \frac{\sigma}{p^*} \frac{\partial p^*}{\partial x} \frac{\partial p'}{\partial \sigma} \right] + p^* fv - p^* ew \cos \theta + D_u \quad (1)$$

194
 195

$$\frac{\partial p^* v}{\partial t} = -m^2 \left[\frac{\partial p^* uv/m}{\partial x} + \frac{\partial p^* vv/m}{\partial y} \right] - \frac{\partial p^* v \dot{\sigma}}{\partial \sigma} + vDIV - \frac{mp^*}{\rho} \left[\frac{\partial p'}{\partial y} - \frac{\sigma}{p^*} \frac{\partial p^*}{\partial y} \frac{\partial p'}{\partial \sigma} \right] - p^* fu + p^* ew \sin \theta + D_v \quad (2)$$

196

197

$$\frac{\partial p^* w}{\partial t} = -m^2 \left[\frac{\partial p^* u w / m}{\partial x} + \frac{\partial p^* v w / m}{\partial y} \right] - \frac{\partial p^* w \dot{\sigma}}{\partial \sigma} + w DIV +$$

$$p^* g \frac{\rho_0}{\rho} \left[\frac{1}{p^*} \frac{\partial p'}{\partial \sigma} + \frac{T'_v}{T} - \frac{T_0 p'}{T p_0} \right] - p^* g [(q_c + q_r)] + p^* e (u \cos \theta - v \sin \theta) + D_w \quad (3)$$

198

199

$$\frac{\partial p^* p'}{\partial t} = -m^2 \left[\frac{\partial p^* u p' / m}{\partial x} + \frac{\partial p^* v p' / m}{\partial y} \right] - \frac{\partial p^* p' \dot{\sigma}}{\partial \sigma} + p' DIV -$$

$$m^2 p^* \gamma p \left[\frac{\partial u / m}{\partial x} - \frac{\sigma}{m p^*} \frac{\partial p^*}{\partial x} \frac{\partial u}{\partial \sigma} + \frac{\partial v / m}{\partial y} - \frac{\sigma}{m p^*} \frac{\partial p^*}{\partial y} \frac{\partial v}{\partial \sigma} \right] + \rho_0 g \gamma p \frac{\partial w}{\partial \sigma} + p^* \rho_0 g \quad (4)$$

200

201

$$\frac{\partial p^* T}{\partial t} = -m^2 \left[\frac{\partial p^* u T / m}{\partial x} + \frac{\partial p^* v T / m}{\partial y} \right] - \frac{\partial p^* T \dot{\sigma}}{\partial \sigma} + T DIV +$$

$$\frac{1}{\rho c_p} \left[p^* \frac{D p'}{D t} - \rho_0 g p^* w - D_{p'} \right] + p^* \frac{\dot{Q}}{c_p} + D_T \quad (5)$$

202

203

204 Where:

$$DIV = m^2 \left[\frac{\partial p^* u / m}{\partial x} + \frac{\partial p^* v / m}{\partial y} \right] + \frac{\partial p^* \dot{\sigma}}{\partial \sigma}$$

205

$$\dot{\sigma} = -\frac{\rho_0 g}{p^*} w - \frac{m \sigma}{p^*} \frac{\partial p^*}{\partial x} u - \frac{m \sigma}{p^*} \frac{\partial p^*}{\partial y} v$$

206

$$\tan \theta = -\cos \phi \frac{\partial \lambda / \partial y}{\partial \phi / \partial x}$$

207

$$p(x, y, z, t) = p_0(z) + p'(x, y, z, t)$$

$$T(x, y, z, t) = T_0(z) + T'(x, y, z, t)$$

$$\rho(x, y, z, t) = \rho_0(z) + \rho'(x, y, z, t)$$

208

209

210 with the vertical sigma coordinate defined as:

211

$$\sigma = \frac{(p_0 - p_t)}{(p_s - p_t)}$$

212

213

214 p_s is the surface pressure and p_0 is the reference pressure profile. The total pressure

215 at each grid point is thus given as:

216

$$217 \quad p(x, y, z, t) = p^* \sigma(k) + p_t + p'(x, y, z, t)$$

218

219 With p_t being the top model pressure assuming a fixed rigid lid.

220 The model physics schemes for boundary layer, radiative transfer, land and ocean
221 surface processes, cloud and precipitation processes are extensively described in Giorgi
222 et al. (2012) and summarized in Table 1. For each physics component a number of
223 parameterization options are available (Table 1), and can be selected using a switch
224 selected by the user. As mentioned, the use of non-hydrostatic dynamics is especially
225 important when going to convection-permitting resolutions of a few km (Prein et al. 2015).
226 At these resolutions the scale separation assumption underlying the use of cumulus
227 convection schemes is not valid any more, and explicit cloud microphysics
228 representations are necessary. The RegCM4 currently includes two newly implemented
229 microphysics schemes, the Nogherotto-Tompkins (Nogherotto et al. 2016) and the WSM5
230 scheme from the Weather Research Forecast (WRF, Skamarok et al. 2008) model, which
231 are briefly described in the next sections for information to model users.

232

Model physics (<i>Namelist flag</i>)	Options	<i>n. option</i>	Reference
Dynamical core (<i>idynamic</i>)	Hydrostatic	1	Giorgi et al. 1993a,b Giorgi et al. 2012
	Non-Hydrostatic (*)	2	present paper
Radiation (<i>irrtm</i>)	CCSM	0	Kiehl et al. 1996
	RRTM (*)	1	Mlawer et al. 1997
Microphysics	Subex	1	Pal et al 2000

<i>(ipptls)</i>	Nogherotto Thompkins	2	Nogherotto et al. 2016
	WSM5 (*)	3	Hong et al 2004
Cumulus <i>(icup)</i>	Kuo	1	Anthes et al. 1987
	Grell	2	Grell 1993
	Emanuel	4	Emanuel 1991
	Tiedtke	5	Tiedtke 1989, 1993
	Kain-Fritsch	6	Kain and Fritsch, 1990; Kain 2004
	MM5 Shallow cumulus (only mixing) (*)	-1	Grell et al. 1994
Planetary Boundary Layer <i>(ibltyp)</i>	Modified-Holtslag	1	Holtslag et al., 1990
	UW	2	Bretherton et al. 2004
Land Surface <i>(code compiling option)</i>	BATS	/	Dickinson et al. 1993; Giorgi et al. 2003
	CLM4.5	/	Oleson et al. 2013
Ocean Fluxes <i>(iocnflx)</i>	BATS	1	Dickinson et al. 1993
	Zeng	2	Zeng et al. 1998
	COARE	3	Fairall et al. 1996a,b

Interactive lake (<i>lakemod</i>)	1D diffusion/convection	1	Hostetler et al. 1993
Tropical band (<i>i_band</i>)	RegT-Band	1	Coppola et al. 2012
Coupled ocean (<i>iocncpl</i>)	RegCM-ES	1	Sitz et al. 2017

233 **Table 1 Core and sub-grid physics scheme available in RegCM-NH. New schemes**
234 **available with this release are starred (*).**

235

236

237 **Explicit microphysics schemes**

238 ***Nogherotto-Tompkins Scheme***

239 A new parameterization for explicit cloud microphysics and precipitation built upon the
240 European Centre for Medium Weather Forecast's Integrated Forecast System (IFS)
241 module (Tiedtke [1993], Tompkins [2007]), was introduced in RegCM4 (*ipptls* = 2 in
242 *µparam*) by Nogherotto et al. [2016]. In the present configuration, the scheme
243 implicitly solves 5 prognostic equations for water vapor, *qv*, cloud liquid water, *ql*, rain, *qr*,
244 cloud ice, *qi*, and snow, *qs*, but it is also easily extendable to a larger number of variables.
245 Water vapor, cloud liquid water, rain, cloud ice and snow are all expressed in terms of the
246 grid-mean mixing ratio.

247 Cloud liquid and ice water content are independent, allowing the existence of supercooled
248 liquid water and mixed-phase clouds. Rain and snow precipitate with a fixed terminal fall
249 speed and can then be advected by the three dimensional winds. A check for the
250 conservation of enthalpy and of total moisture is ensured at the end of each timestep. The
251 governing equation for each variable is:

252

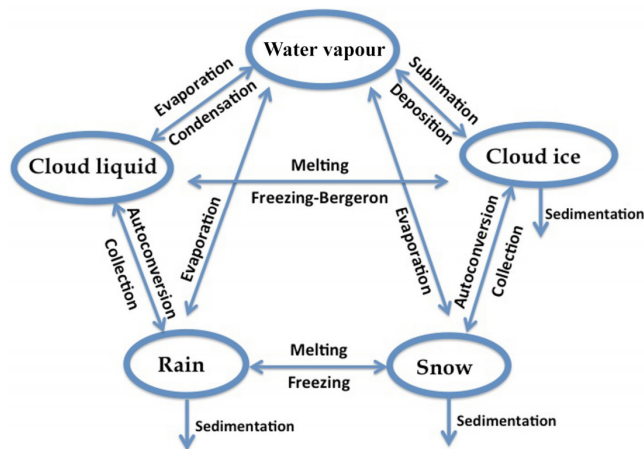
$$\frac{\partial q_x}{\partial t} = S_x + \frac{1}{\rho} \frac{\partial}{\partial z} (\rho V_x q_x)$$

253

254

255 The local variation of the mixing ratio q_x of the variable x is given by the sum of
 256 S_x , containing the net sources and sinks of q_x through microphysical processes (i.e.
 257 condensation, evaporation, auto-conversion, melting, etc.), and the sedimentation term,
 258 which is a function of the fall speed V_x . An upstream approach is employed to solve the
 259 equations. The sources and sinks contributors are divided in two groups according to the
 260 duration of the process they describe: processes that are considered to be fast relative to
 261 the model time step are treated implicitly while slow processes are treated explicitly. The
 262 processes taken into account (shown in Figure 2) are the microphysical pathways across
 263 the 5 water variables: condensation, autoconversion, evaporation, cloud water collection
 264 (accretion), and autoconversion for warm clouds, and freezing, melting, deposition,
 265 sublimation for cold clouds.

266



267

268 **Figure 2: Depiction of the new scheme, showing the five prognostic variables and**
 269 **how they are related to each other through microphysical processes**

270 For each microphysical pathway, phase changes are associated with the release or
 271 absorption of latent heat, which then impacts the temperature budget. The impact is

272 calculated using the conservation of liquid water temperature TL defined as:
273

$$274 \quad T_L = T - \frac{L_v}{C_p}(q_l + q_r) - \frac{L_s}{C_p}(q_i + q_s).$$

275 Given that $dTL = 0$, the rate of change of the temperature is given by the following
276 equation:

277

$$278 \quad \frac{\partial T}{\partial t} = \sum_{x=1}^m \frac{L(x)}{C_p} \left(\frac{dq_x}{dt} - D_{q_x} - \frac{1}{\rho} \frac{\partial}{\partial z} (\rho V_x q_x) \right)$$

279

280 where $L(x)$ is the latent heat of fusion or evaporation, depending on the process
281 considered, D_{q_x} is the convective detrainment and the third term in brackets is the
282 sedimentation term.

283 At the end of each time step a check is carried out of the conservation of total water and
284 moist static energy: $h = C_p T + gz + Lq_x$.

285 The scheme is tunable through parameters in the *µparam* section of the namelist
286 (RegCM-4.7.1/Doc/README.namelist; Elguindi et al. 2017).

287

288 **WSM5 Scheme**

289 RegCM4-NH also employs the Single-Moment 5-class microphysics scheme of the WRF
290 model (Skamarock et al., 2008). This scheme (ipptls = 3 in µparam) follows Hong
291 et al. (2004) and, similarly to Nogherotto et al. (2016), includes vapor, rain, snow, cloud
292 ice, and cloud water hydrometeors. The scheme separately treats ice and water
293 saturation processes, assuming water hydrometeors for temperatures above freezing,
294 and cloud ice and snow below the freezing level (Dudhia, 1989, Hong et al., 1998). It
295 accounts for supercooled water and a gradual melting of snow below the melting layer
296 (Hong et al., 2004, and Hong and Lim, 2006). Therefore, the WSM5 and Nogherotto-
297 Tompkins schemes have similar structures (Figure 2), but also important differences.

298 Differently from the Nogherotto-Tompkins scheme, the WSM5 (as well as the other WSM
299 schemes in WRF) prescribes an inverse exponential continuous distribution of particle
300 size (ex. Marshall and Palmer (1948) for rain, Gunn and Marshall (1958) for snow). It also
301 includes the size distribution of ice particles and, as a major novelty, the definition of the
302 number of ice crystals based on ice mass content rather than temperature. Both the
303 Nogherotto-Tompkins and WSM5 schemes include autoconversion, i.e. sub-time step
304 processes of conversion of cloud water to rain and cloud ice to snow. For rain, Hong et
305 al. (2004) use a Kessler (1969) type algorithm in WSM5, but with a stronger physical basis
306 following Tripoli and Cotton (1980). The Nogherotto-Tompkins scheme also includes the
307 original Kessler (1969) formula as an option, but it makes available other three
308 exponential approaches following Sundqvist et al. (1989), Beheng (1994), and
309 Khairoutdinov and Kogan (2000). For ice autoconversion the Nogherotto-Tompkins
310 scheme uses an exponential approach (Sundqvist, 1989) with a specific coefficient for ice
311 particles (following Lin et al., 1983) depending on temperature, while the WSM5 uses a
312 critical value of ice mixing ratio (depending on air density) and a maximum allowed ice
313 crystal mass (following Rutledge and Hobbs, 1983) that suppresses the process at low
314 temperatures because of the effect of air density. Finally, the WSM5 has no dependency
315 on cloud cover for condensation processes while the Nogherotto-Tompkins scheme uses
316 cloud cover to regulate the condensation rate in the formation of stratiform clouds.

317 ***Illustrative case studies***

318

319 Three case studies (Table 2) of Heavy Precipitation Events (HPE) have been identified in
320 order to test and illustrate the behavior of the non-hydrostatic core of the RegCM4-NH,
321 with focus on the explicit simulation of convection over different regions of the world. In
322 two of the test cases, California and Lake Victoria, data from the ERA-Interim reanalysis
323 (Dee et al. 2011) are used to provide initial and lateral meteorological boundary conditions
324 (every 6 hours) for an intermediate resolution run (grid spacing of 12 km, with use of
325 convection parameterizations), which then provides driving boundary conditions for the
326 convection-permitting experiments (Figure 3). In the Texas case study, however, we
327 nested the model directly in the ERA-Interim reanalysis given that such configuration
328 was able to accurately reproduce the HPE intensity. In this case the model uses a large
329 LBC relaxation zone which allows the description of realistic fine-scale features driving
330 this weather event (although not fully consistent with the Matte et al. (2017) criteria). All
331 simulations start 24-48 hours before the HPE (Table 2). The analysis focuses on the total
332 accumulated precipitation over the entire model domain at 3 km resolution (Figure 2) for
333 the periods defined in Table 2. In the cases of California and Texas the evaluation also
334 includes the time series of 6 hourly accumulated precipitation averaged on the region of
335 maximum precipitation (black rectangles in Figures 5a and 7a) because high temporal
336 resolution observations (NCEP/CPC) are also available (Table 3). The discussion of the
337 case studies is presented in the next sections; the configuration files (namelists) with full
338 settings for the three test cases are available at <https://zenodo.org/record/5106399>.

339

340 A key issue concerning the use of CP-RCMs is the availability of very high resolution,
341 high quality observed datasets for the assessment and evaluation of the models, which
342 is lacking for most of the world regions. Precipitation measurements come from
343 essentially three distinct sources: in-situ rain-gauges, ground radar and satellite. In the
344 present study we use 7 observational datasets depending on the case study and the area
345 covered, as described in Table 3. We have used: Precipitation Estimation from Remotely
346 Sensed Information using Artificial Neural Networks - Climate Data Record (PERSIAN-
347 CDR), Climate Hazards Group InfraRed Precipitation with Station data (CHIRPS), the
348 Climate Prediction Center morphing method (CMORPH), Tropical Rainfall Measuring
349 Mission (TRMM), NCEP/CPC-Four Kilometer Precipitation Set Gauge and Radar

350 (NCEP/CPC), CPC-Unified gauge-based daily precipitation estimates (CPC) and
 351 Parameter-elevation Regressions on Independent Slopes Model (PRISM) (Table 3).
 352 NCEP/CPC is a precipitation analysis which merges a rain gauge dataset with radar
 353 estimates. CMORPH and PERSIAN-CDR are based on satellite measurements, CHIRPS
 354 incorporates satellite imagery with in-situ station data. CPC is a gauge-based analysis of
 355 daily precipitation. The PRISM dataset gathers climate observations from a wide range
 356 of monitoring networks, applying sophisticated quality control measures and developing
 357 spatial climate datasets which incorporate a variety of modeling techniques at multiple
 358 spatial and temporal resolutions.

359

Case	ACRONYM	Region of The event	Domains size lon x lat x vertical levels	Simulation Time Window (UTC)
1	CAL	California	480 x 440 x 41	15 Feb 2004 00:00 19 Feb 2004 00:00
2	TEX	Texas	480 x 440 x 41	9 June 2010 00:00 12 June 2010 00:00
3	LKV	Lake Victoria	550 x 530 x 41	25 Nov 1999 00:00 1 Dec 1999 00:00

360 **Table 2: List of acronyms and description of the test cases with corresponding**
 361 **3km domain sizes and simulation period.**

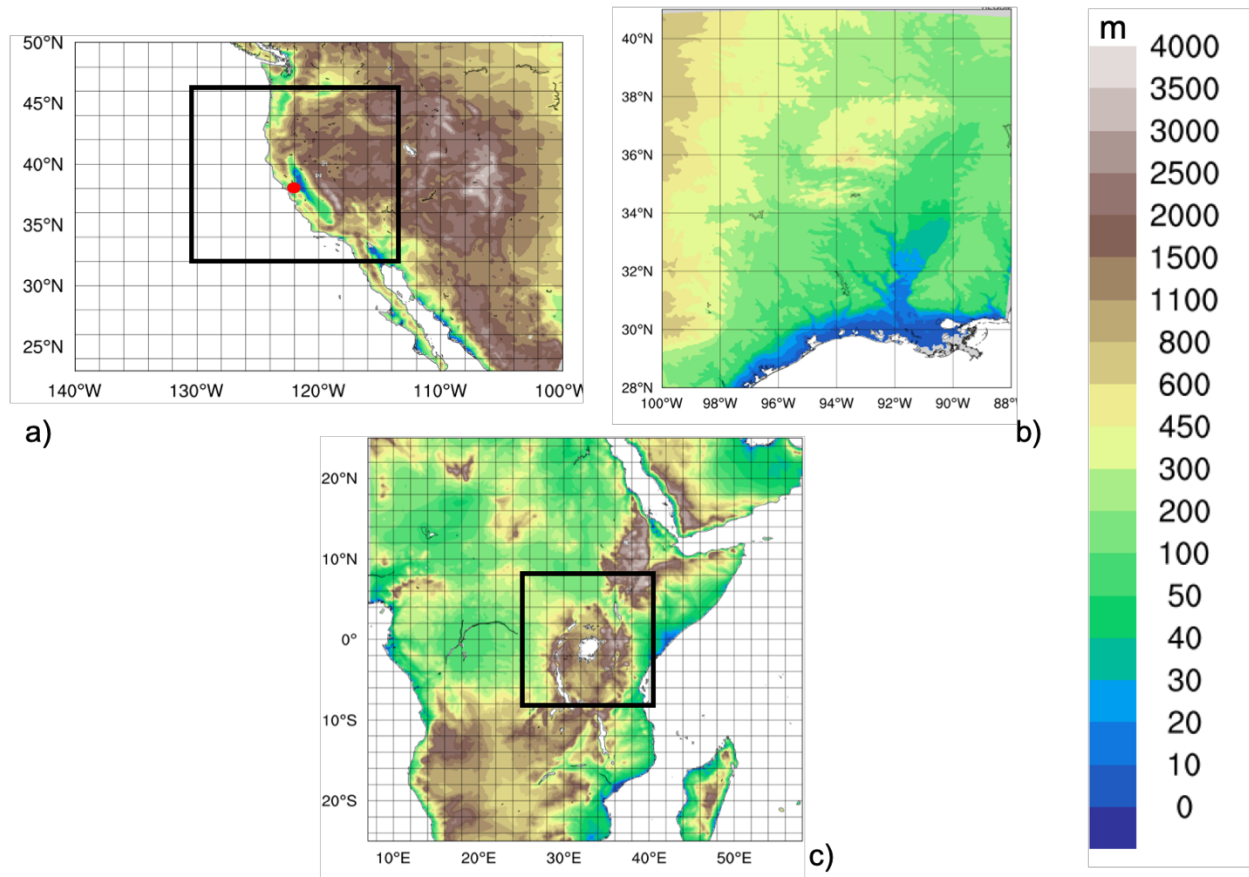
362

Dataset name	Region	Spatial Resolution	Temporal Resolution	Data Source	Reference
TRMM	World	0.5°	Daily	Satellite	Huffman et al. (2007)

CHIRPS	World	0.05°	Daily	Station data+Satellite	Funk et al. (2015)
CMORPH	World	0.25°	Daily	Satellite	Joyce et al. (2004)
NCEP/CPC	USA	0.04°	Hourly	<i>Gauge and Radar</i>	https://doi.org/10.5065/D69Z93M3 . Accessed: 27/06/2018
CPC	World	0.5°	Daily	Station data	Chen and Xie (2008)
PRISM	USA	0.04°	Daily	Station data	PRISM Climate Group. 2016.
PERSIAN-CDR	World	0.25°	Daily	Satellite	Ashouri et al. (2015)

363 **Table 3: List of observed precipitation datasets used for comparison.**

364



365

366 **Figure 3: Domains tested , a) California (CAL) , b) Texas (TEX), c) Lake Victoria**
 367 **(LKV) . For CAL (a) and LKV (b) the black square shows the 3 km simulation**
 368 **domains nested in the 12 km domain in figure. For TEX case (b) the 3 km domain**
 369 **simulation is fed directly with the ERA-Interim reanalysis fields.**

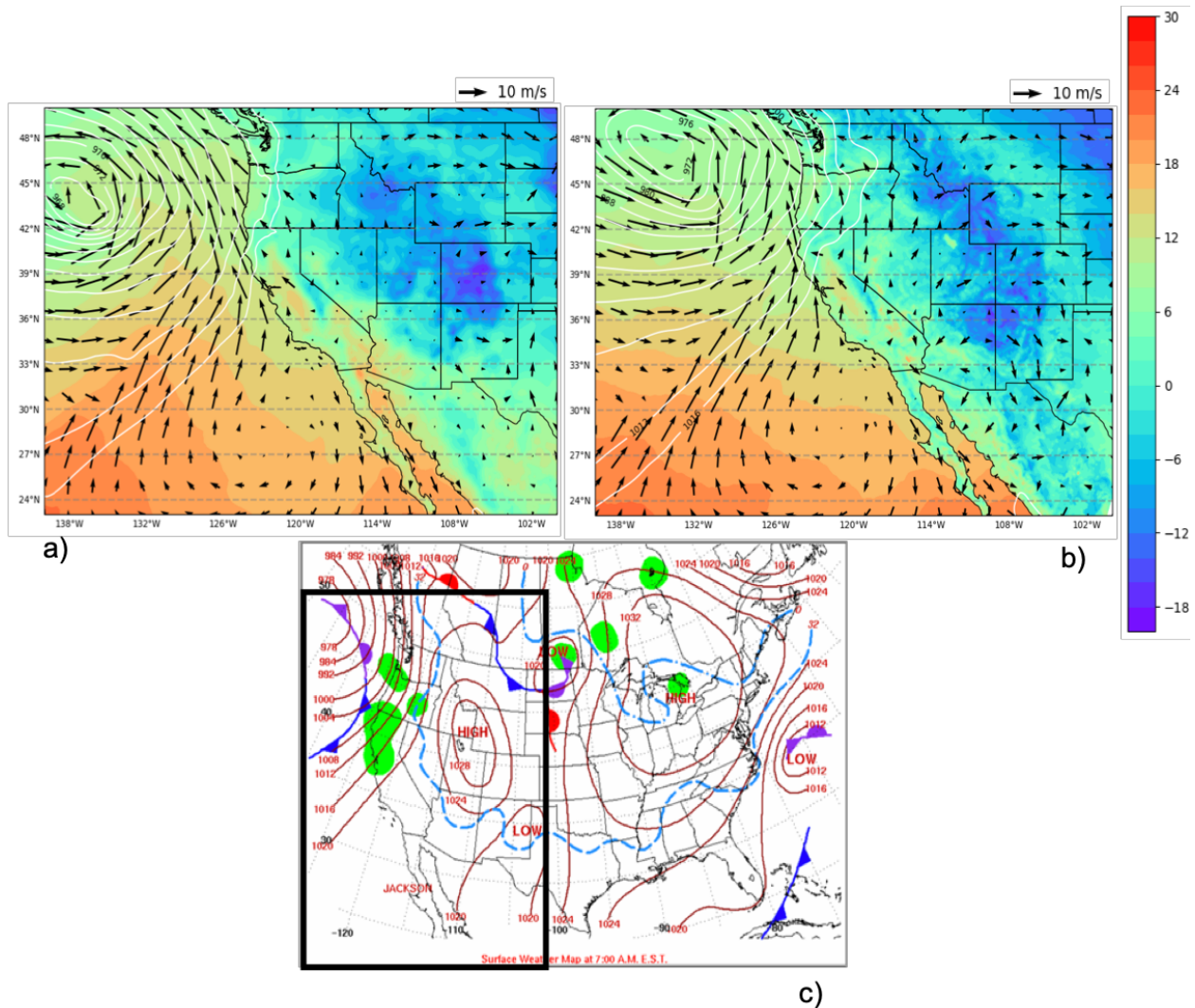
370

371

372 **California**

373 The first case, referred to as CAL in Table 2, is a HPE which occurred on February 16-18
 374 2004, producing flooding conditions for the Russian River, a southward-flowing river in
 375 the Sonoma and Mendocino counties of northern California (red-dot in Figure 3a). The
 376 event is documented in detail by Ralph et al. (2006), who focused their attention on the
 377 impact of narrow filament-shaped structures of strong horizontal water vapor transport

378 over the eastern Pacific Ocean and the western U.S. coast, called Atmospheric Rivers
 379 (ARs). ARs are typically associated with a low-level jet stream ahead of the cold front of
 380 extratropical cyclones (Zhu and Newell 1998; Dacre et al. 2015; Ralph et al. 2018), and
 381 can induce heavy precipitation where they make landfall and are forced to rise over
 382 mountain chains (Gimeno et al. 2014). The CAL event consists of a slow propagating
 383 surface front arching southeastward towards Oregon and then southwestward offshore
 384 of California (Figure 4a,c). Rain began over the coastal mountains of the Russian River
 385 watershed at 0700 UTC of February 16, as a warm front descended southward, and also
 386 coincided with the development of orographically favoured low-level upslope flow (Ralph
 387 et al., 2006).



388

389 **Figure 4: a,b) mean sea level pressure (mslp, hPa, white contour lines), surface**
390 **temperature (color shading, °C) and 100-m wind direction (black arrows, m/s) at 0700 UTC,**
391 **February 16, 2004 of ERA5 reanalysis and RegCM 12km respectively. c) NCEP-NOA**
392 **Surface Analysis of pressure and fronts. The black box in (c) bounded the area represented**
393 **in (a) and (b)**

394 The intermediate resolution (12 km) domain (Figure 3a) covers a wide area
395 encompassing California and a large portion of the coastal Pacific Ocean, with 23 vertical
396 levels and a parameterization for deep convection based on the Kain–Fritsch scheme
397 (Kain, 2004). The ERA-Interim driven simulation is initialized at 0000 UTC, February 15
398 2004 (Table 2) and lasts until 0000 UTC February 19 2004. This simulation is used as a
399 boundary conditions for a RegCM4-NH run over a smaller area centered over northern
400 California (Fig. 3a) at 3 km horizontal resolution, with 41 vertical levels and boundary
401 conditions updated every 6 hours. In RegCM4-NH only the shallow convection code of
402 the Tiedtke scheme (Tiedtke, 1996) is activated. Simulated precipitation is compared
403 with the CHIRPS, CMORPH, TRMM, PRISM, NCEP/CPC observations (Table 3).

404 As shown in Figure 4 the February 16 synoptic conditions for mean sea level pressure
405 (mslp), surface temperature and wind direction of this case study, are well reproduced by
406 RegCM4 at 12 km (Fig. 4b) when compared to ERA5 reanalysis (Fig. 4a). The surface
407 analysis of pressure and fronts derived from the operational weather maps prepared at
408 the National Centers for Environmental Prediction, Hydrometeorological Prediction
409 Center, National Weather Service
410 (https://www.wpc.ncep.noaa.gov/dailywxmap/index_20040216.html) is also reported in
411 Figure 4c.

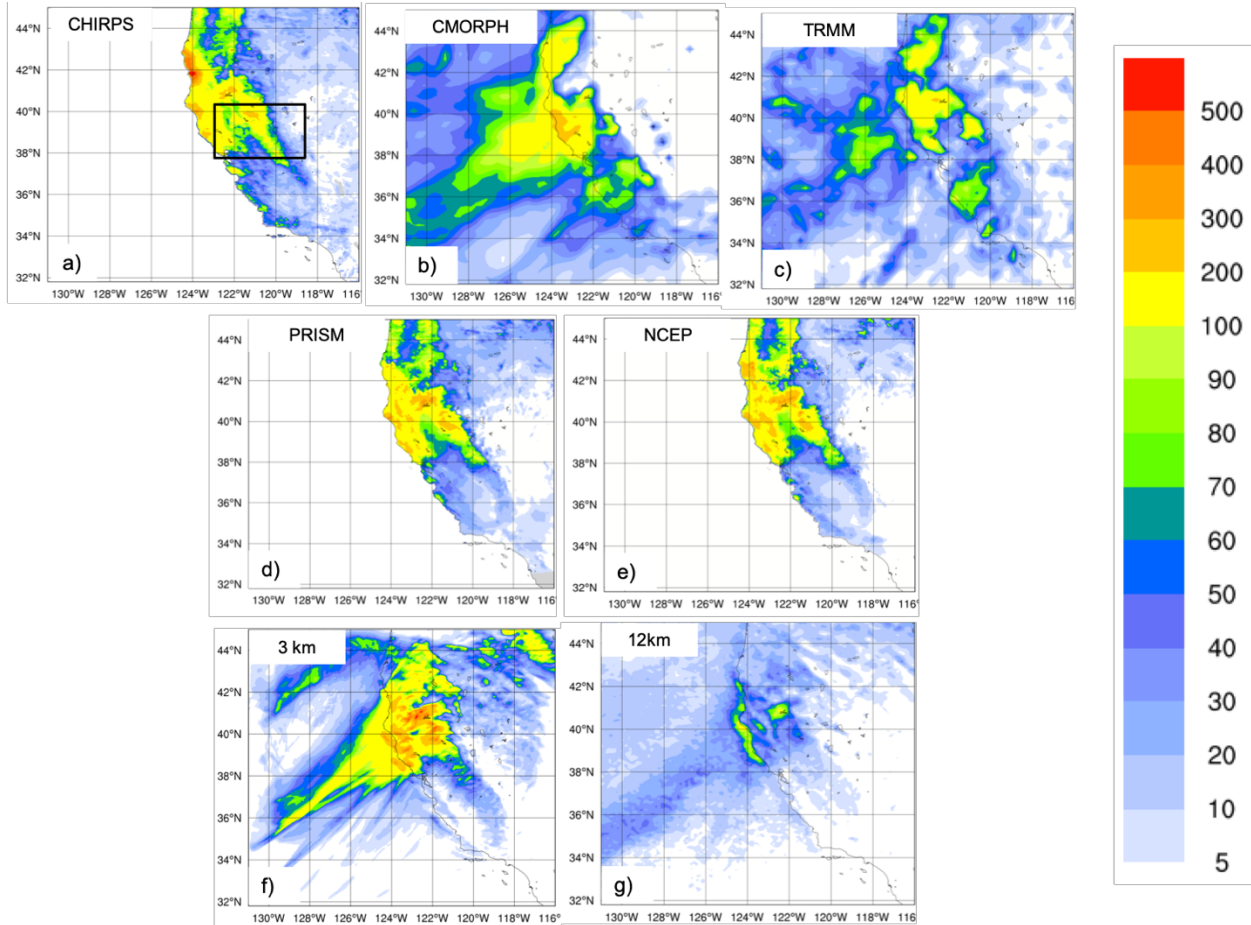
412 The available observed precipitation datasets show similar patterns for the total
413 accumulated precipitation (Figure 5), in particular CHIRPS (Figure 5a), PRISM (Figure
414 5d) and NCEP (Figure 5e) exhibit similar spatial details and magnitudes of extremes.
415 CHIRPS shows a maximum around 42°N which is not found in the other datasets.
416 CMORPH (Figure 5b) and TRMM (Figure 5c) show lower precipitation maxima and lesser
417 spatial details due to their lower resolution, indicating that the performance of satellite-

418 based products may be insufficient as a stand alone product to validate the model for this
419 case.

420 The largest observed maxima are placed on the terrain peaks, with extreme rainfall
421 greater than 250 mm in 60 hours over the coastal mountains and between 100 – 175 mm
422 elsewhere (Fig. 5). The black box in Fig 5a shows the area of the Russian River
423 watershed where the largest rainfall rates were detected (269 mm and 124 mm in 60-h
424 accumulated rainfall between 0000 UTC February 16 and 1200 UTC February 18, 2004,
425 respectively) (Ralph et al., 2006).

426 The convection-permitting simulation captures the basic features of the observed
427 precipitation, both in terms of spatial distribution (Fig. 5f) and of temporal evolution of
428 rainfall (Fig. 6a). However, it shows higher precipitation rates than observed over the sea
429 and over the mountain chains, with lower intensities than observed in the south-east part
430 of the mountain chain (Fig. 5). The 12-km simulation instead severely underestimates the
431 magnitude of the event (Fig. 5g).

432 Figure 6a shows the 6-hourly accumulated precipitation averaged over the black box in
433 Figure 5a. The 3 km and 12 km simulations capture the onset of the event, but the peak
434 intensity is strongly underestimated by the 12 km run, while it is well simulated by the 3
435 km run, although the secondary maximum is overestimated. These results demonstrate
436 that only the high resolution convection-permitting model is able to captures this extreme
437 event, and that parameterized convection has severe limits in this regard (Done et al.
438 2004; Lean et al. 2008; Weisman et al. 2008; Weusthoff et al. 2010; Schwartz 2014; Clark
439 et al. 2016).



440

441 **Figure 5 : Total accumulated precipitation (mm) during the California case: CHIRPS (a),**
 442 **CMORPH (b), TRMM (c) observations, PRISM (d) and NCEP Reanalysis (e) and convection-**
 443 **permitting simulation with RegCM4-NH at 3km (f) and RegCM4 at 12km (g). The black box**
 444 **denotes the area where the spatial average of 6-hourly accumulated precipitation is**
 445 **calculated for Figure 6a.**

446

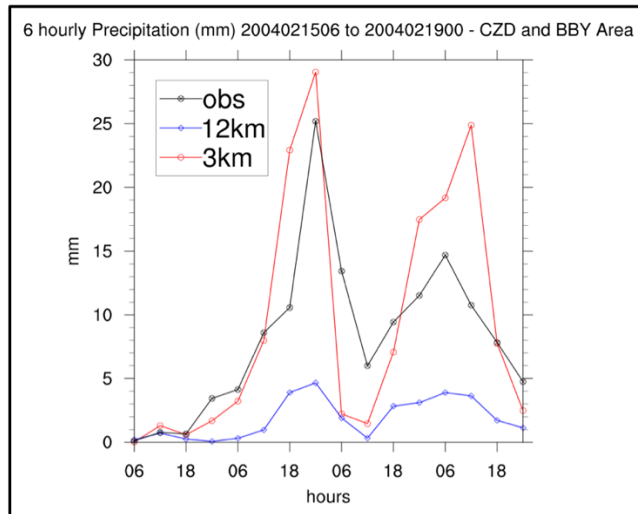
447

448

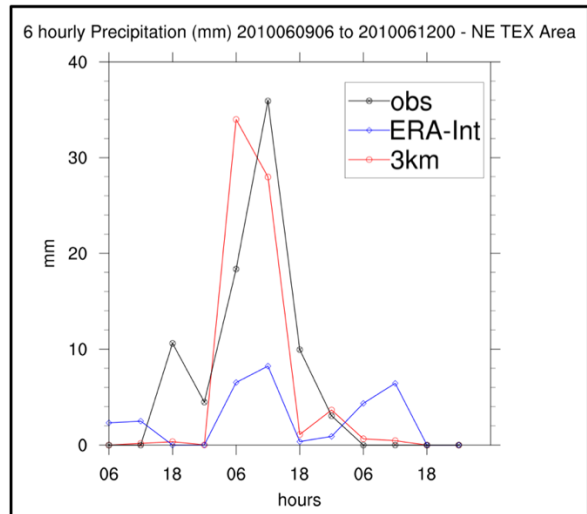
449

450

CAL (a)



TEX (b)



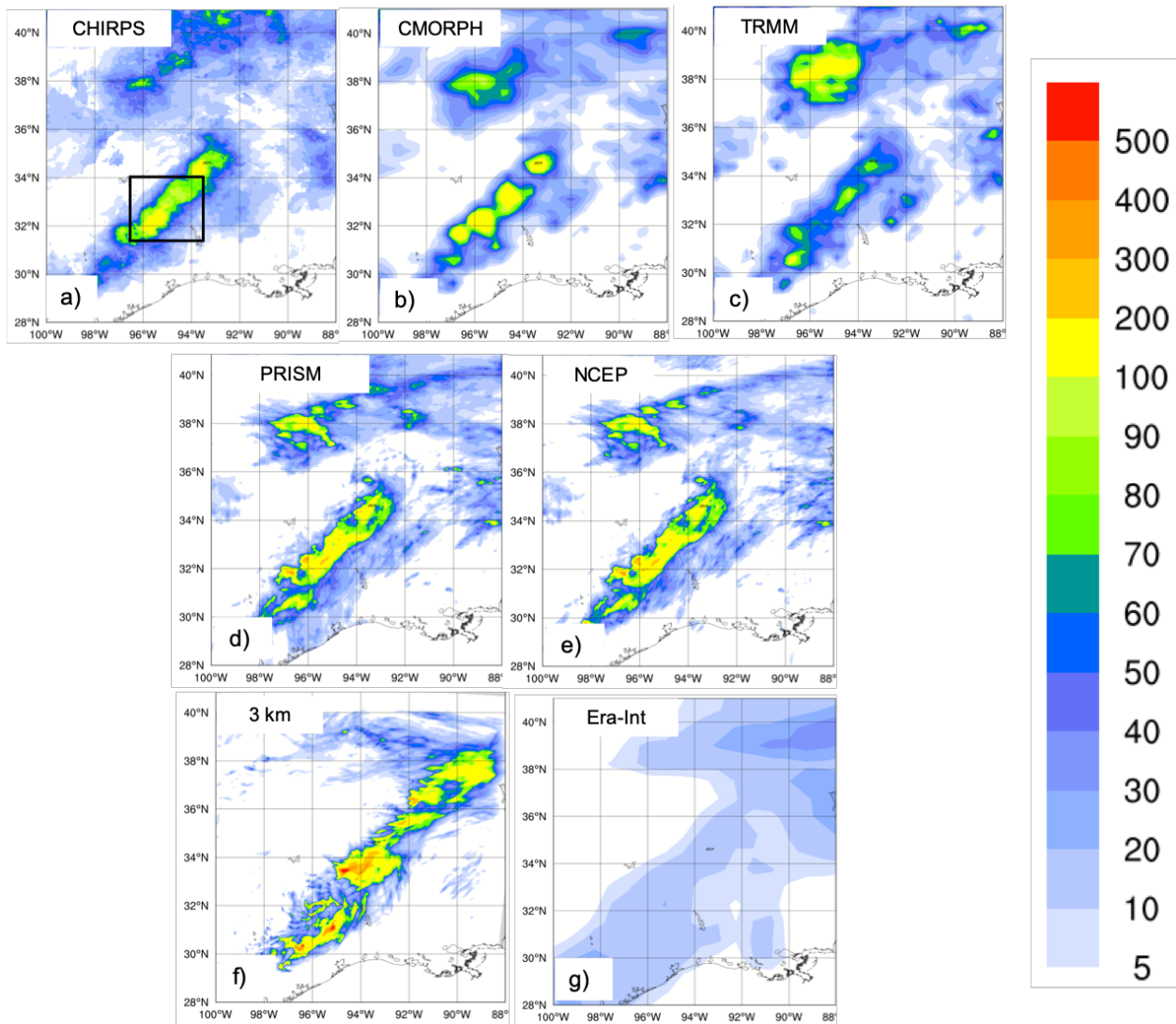
451

452 **Figure 6: Time series of the 6 hourly accumulated precipitation (in mm on the y-axis) during**
 453 **the CAL event (a) and during the TEX event (b). The blue lines show RegCM4 12 Km and**
 454 **ERA interim 6 hourly accumulated precipitation averaged over the areas indicated by the**
 455 **black squares in Figures 5 and 7 while the red line shows the 6 hourly accumulated**
 456 **precipitation simulated by RegCM4-NH. The observations are shown with a black line.**

457

458 Texas

459 Case 2, hereafter referred to as TEX (Table 2), is a convective precipitation episode
 460 exhibiting characteristics of the “Maya Express” flood events, linking tropical moisture
 461 plumes from the Caribbean and Gulf of Mexico to midlatitude flooding over the central
 462 United States (Higgins 2011). During the TEX event, an upper-level cutoff low over
 463 northeastern Texas, embedded within a synoptic-scale ridge, moved slowly
 464 northeastward. Strong low-level flow and moisture transport from the western Gulf of
 465 Mexico progressed northward across eastern Texas. The event was characterized by
 466 low-level moisture convergence, weak upper-level flow, weak vertical wind shear, and
 467 relatively cold air (center of cutoff low), which favored the slow-moving convective storms
 468 and nearly stationary thunderstorm outflow boundaries. The main flooding event in
 469 eastern Texas occurred on June 10, 2010, with a daily maximum rainfall of 216.4 mm for
 470 the region in the black box of Figure 7a (Higgins 2011).



471
 472 **Figure 7: Total accumulated precipitation (mm) during the Texas case: CHIRPS (a),**
 473 **CMORPH (b), TRMM (c), PRISM (d), NCEP Reanalysis (e) and convection-permitting**
 474 **simulation with RegCM4-NH at 3 km grid spacing (f) and ERA-Interim (g). The black box (a)**
 475 **shows the area where the spatial average of 6-hourly accumulated precipitation was**
 476 **calculated for Figure 6b**

477 As for the California case, the observed precipitation datasets show coherent patterns for
 478 the total accumulated precipitation (Figure 7), with the highest values related to the
 479 mesoscale convective system in eastern Texas (~ 200 mm), and another smaller area of
 480 high precipitation more to the north, approximately over Oklahoma. PRISM (Figure
 481 7d) and NCEP (Figure 7e) capture similar spatial details and magnitudes of extremes,

482 CHIRPS (Figure 7a) has lower precipitation extremes in the north compared to the other
483 datasets, while CMORPH (Figure 7b) and TRMM (Figure 7c) show the lowest
484 precipitation extremes and reduced spatial details as already noted for the California
485 case.

486 Figure 7f and Figure 7g present precipitation as produced by the RegCM4-NH and the
487 ERA-Interim reanalysis (driving data) respectively. ERA-Interim reproduces some of the
488 observed features of precipitation, but with a substantial underestimation over the areas
489 of maximum precipitation because of its coarse resolution. By comparison, the RegCM4-
490 NH simulation (Fig. 7f) shows an improvement in both pattern and intensity of
491 precipitation, and is substantially closer to observations over eastern Texas. However,
492 the precipitation area is slightly overestimated and the model is not capable of
493 reproducing the small region of maximum precipitation in the north.

494

495 The time series of precipitation over eastern Texas from June 9 to 12, 2010 for
496 observations (black line), ERA-Interim (blue line) and RegCM4-NH (red line) are reported
497 in figure 6b. Precipitation increases over this region from 0000 UTC until it reaches the
498 observed maximum at 1200 UTC, on June 10 (~35 mm), gradually decreasing afterwards
499 until 0600 UTC, on June 11. The RegCM4-NH simulation shows a more realistic temporal
500 evolution than the ERA-Interim, which exhibits an overall underestimation of precipitation.
501 The non-hydrostatic model produces precipitation values closer to the observations,
502 however the simulated maximum is reached 6 hours earlier than observed.

503

504

505 **Lake Victoria**

506 Case 3 focuses on Lake Victoria (LKV), with the purpose of testing RegCM4-NH on a
507 complex and challenging region in terms of convective rainfall. It is estimated that each
508 year 3,000-5,000 fishermen perish on the lake due to nightly storms (Red Cross, 2014).
509 In the Lake Victoria basin, the diurnal cycle of convection is strongly influenced by
510 lake/land breezes driven by the thermal gradient between the lake surface and the
511 surrounding land. As the land warms during the course of the day, a lake breeze is
512 generated which flows from the relatively cooler water towards the warmer land surface.

513 The circulation is effectively reversed at night, when the land surface becomes cooler
514 than the lake surface, leading to convergence over the lake and associated thermal
515 instability.

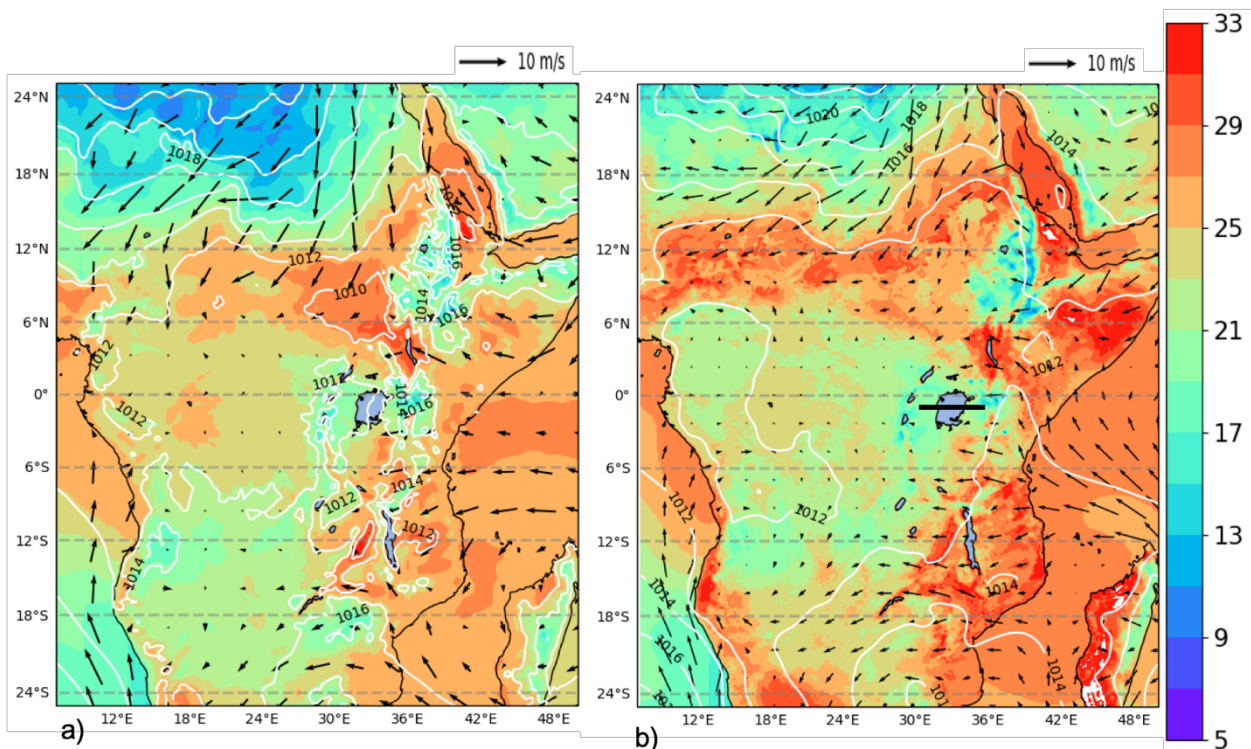
516 In the LKV region, prevailing winds are generally easterly most of the year with some
517 variability due to the movement of the ITCZ. The local diurnal circulation created by the
518 presence of the lake creates two diurnal rainfall maxima. During daylight hours, when the
519 lake breeze begins to advance inland, convergence is maximized on the eastern coast of
520 the lake as the lake breeze interacts with the prevailing easterlies. Studies have also
521 noted the importance of downslope katabatic winds along the mountains to the east of
522 the lake in facilitating convergence along the eastern coastal regions (Anyah et al. 2006).
523 This creates a maximum in rainfall and convection on the eastern coast of LKV.
524 Conversely, during nighttime hours, when the local lake circulation switches to flow from
525 the land towards the lake, the prevailing easterlies create locally strong easterly flow
526 across the lake and an associated maximum in convergence and rainfall on the western
527 side of LKV.

528 The LKV simulation starts on November 25, 1999 and extends to the beginning of
529 December 1999 (Table 2), covering a 5-day period which falls within the short-rain season
530 of East Africa. The choice of 1999, an ENSO neutral year, was made in order to focus the
531 analysis on local effects, such as the diurnal convection cycle in response to the lake/land
532 breeze, with no influence of anomalous large scale conditions. A 1-dimensional lake
533 model (Hostetler et al. 1993; Bennington et al. 2014) interactively coupled to RegCM4-
534 NH was utilized to calculate the lake surface temperature (LST), since lake-atmosphere
535 coupling has been shown to be important for LKV (Sun et al. 2015; Song et al. 2004).
536 This coupled lake model has been already used for other lakes, including Lake Malawi in
537 southern Africa (Diallo et al. 2018). As with the other experiments, the boundary
538 conditions are provided by a corresponding 12 km RegCM4 simulation employing the
539 convection scheme of Tiedtke (1996).

540 At the beginning of the simulation, the LST over the lake is uniformly set to 26°C, and is
541 then allowed to evolve according to the lake-atmosphere coupling. This initial LST value
542 is based on previous studies. For example, Talling (1969) finds Lake Victoria surface

543 temperatures ranging from 24.5-26°C during the course of the year. Several studies have
544 used RCMs to investigate the Lake Victoria climate (Anyah et al., 2006; Anyah and
545 Semazzi 2009, Sun et al. 2015), and found a significant relationship between lake
546 temperature and rainfall depending on season. The value of 26°C is typical of the winter
547 season and was chosen based on preliminary sensitivity tests using different values of
548 initial temperature ranging from 24°C to 26°C.

549 The synoptic feature favorable for the production of precipitation over the LKV in this
550 period corresponds to a large area of southeasterly flow from the Indian Ocean (Fig. 8a),
551 which brings low-level warm moist air into the LKV region facilitating the production of
552 convective instability and precipitation. This synoptic situation, with a low-level south-
553 easterly jet off the Indian Ocean, is a common feature associated with high precipitation
554 in the area (Anyah et al. 2006), and can be seen in ERA5 data (Figure 8a). Although
555 some bias in terms of magnitude, this is reasonably well reproduce by the 12 km
556 simulation (Figure 8b).



557

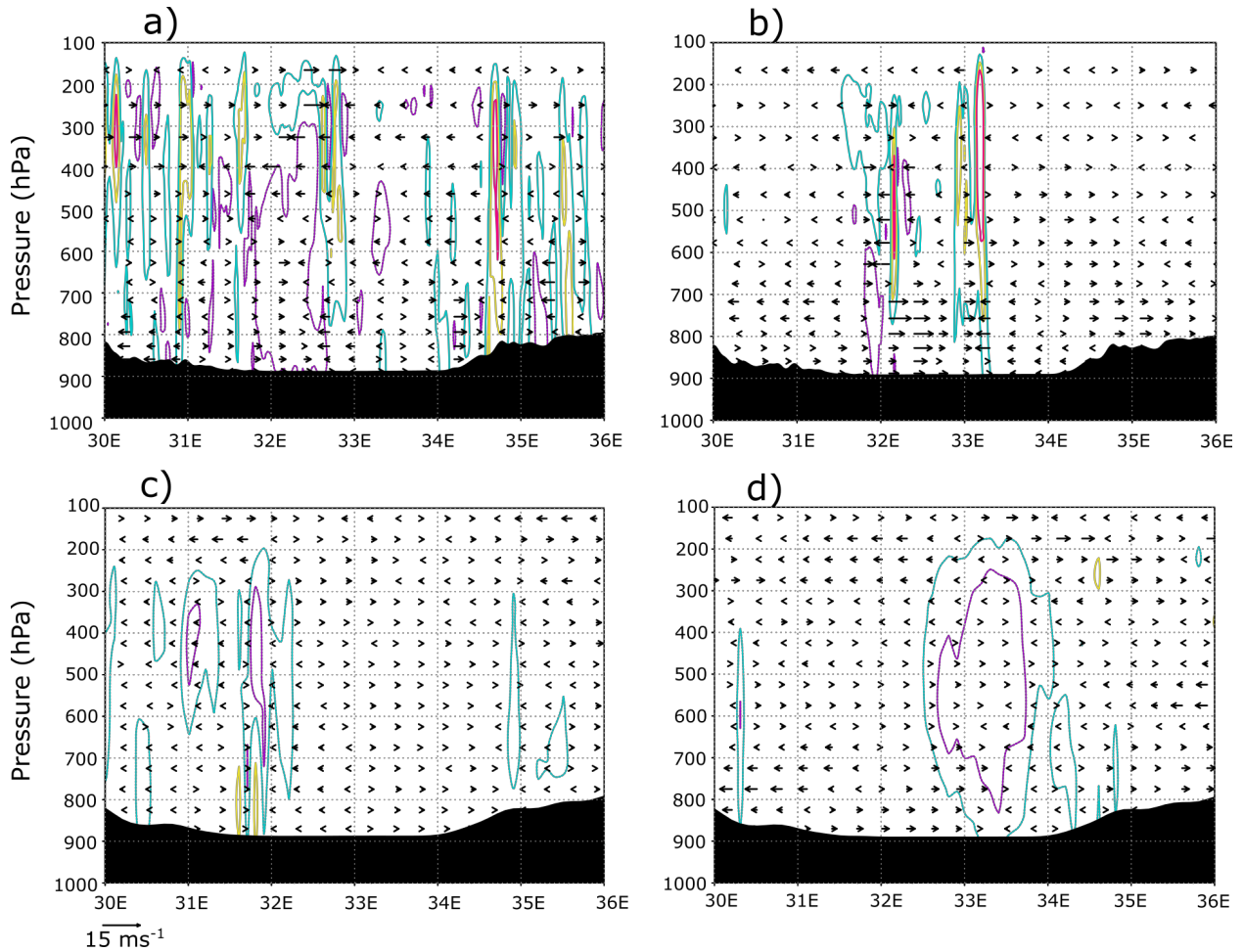
558 **Figure 8: Mean sea level pressure (mslp) (hPa) (white contour lines), surface temperature**
559 **(color shading) (°C) and 100-m wind (black arrows) averaged over the period 25 November**

560 **0000 UTC - 1 December 0000 UTC, by ERA5 reanalysis (a) and RegCM 12km (b). The black**
561 **line (b) shows the cross-section position represented in Fig. 9**

562 The LKV region dynamics are quite distinct between nighttime and daytime and the
563 rainfall in and around the lake has a pronounced diurnal cycle. To understand this strong
564 diurnal cycle, Figure 9 shows a cross-section through the lake (32E to 34E, black line in
565 right panel of Fig. 8b) along 1°S latitude at a period during strong nighttime (Fig. 9b,d;
566 0600Z November 30) and daytime convection (Figure 9a,c; 12Z November 29). Wind
567 vectors in Figure 9 show the zonal-wind anomaly across 0°-2°S to highlight the
568 circulations associated with LKV. During the day, surface heating around the lake leads
569 to a temperature difference between the land and lake sufficient to generate a lake
570 breeze, which causes divergence over the lake, while over the highlands to the east the
571 environment is more conducive to convection where convergence is focused (9a,c).
572 Conversely, during the night, a land breeze circulation is generated, which induces
573 convergence and convection over the lake (Figure 9b,d). In Figure 10, the evolution of
574 the nighttime land breeze is illustrated with cooler temperature anomalies propagating
575 westward onto the lake during the night.

576 Comparing the 3 km simulation to the 12 km forcing run, we find that the localized
577 circulations created by local forcings (i.e. convection) are much stronger in the convection
578 permitting resolution experiment. We also find stronger and more localized areas of
579 convective updrafts compared to the 12 km simulation (Figure 9c,d; omega is shown
580 instead of vertical velocity here because of the difference in dynamical core). As an
581 example during the nighttime event (Figure 9b,d) there is a broad area of upward motion
582 over the lake and the associated broad convergence in the 12km simulation, while in the
583 convection permitting 3km simulation, convection is much more local and concentrated
584 over the western part of the lake. Indeed, nighttime rainfall tends to be concentrated over
585 the western part of the lake (Sun et al. 2015; Figure 11a-d). Stronger convection
586 simulated in the 3 km experiment could also be tied to stronger temperature anomalies
587 shown over the lake and land and between day and night relative to the 12km simulation
588 (Figure 10). The 3km simulation also shows a more pronounced land breeze propagation
589 at night compared to the 12km simulation.

590 This demonstrates that the 3km simulation is better equipped to simulate the localized
 591 circulations associated with this complex land-lake system.

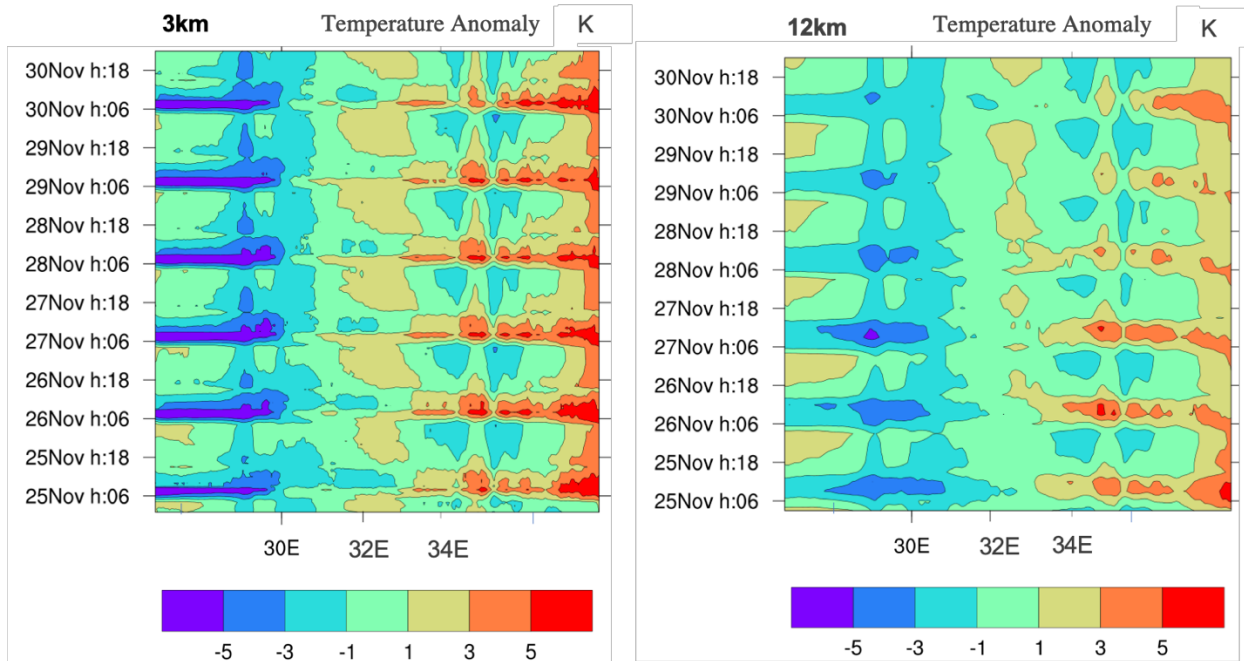


592

593

594 **Figure 9. Cross-section through 1°S (black line in Fig. 8b) of the zonal-wind anomaly (0°-**
 595 **2°S) vectors and the mean contoured vertical velocity (m/s) over 0°-2°S at a) 12Z 29**
 596 **November and b) 6Z 30 November from the 3km simulation. Purple dashed contours**
 597 **indicate -0.1 m/s, light blue contours indicate 0.1 m/s, yellow contours indicate 0.3 m/s,**
 598 **and red contours indicate 0.5 m/s. Lake Victoria encompasses about 32°E to 34°E. The**
 599 **bottom 2 panels show the same as in a) and b) but from the 12km simulation at c) 12Z 29**
 600 **November and d) 6Z 30 November. Purple dashed contours indicate -0.01 hPa/s, light blue**
 601 **dashed contours indicate -0.005 hPa/s, and yellow dashed contours indicate 0.005 hPa/s.**

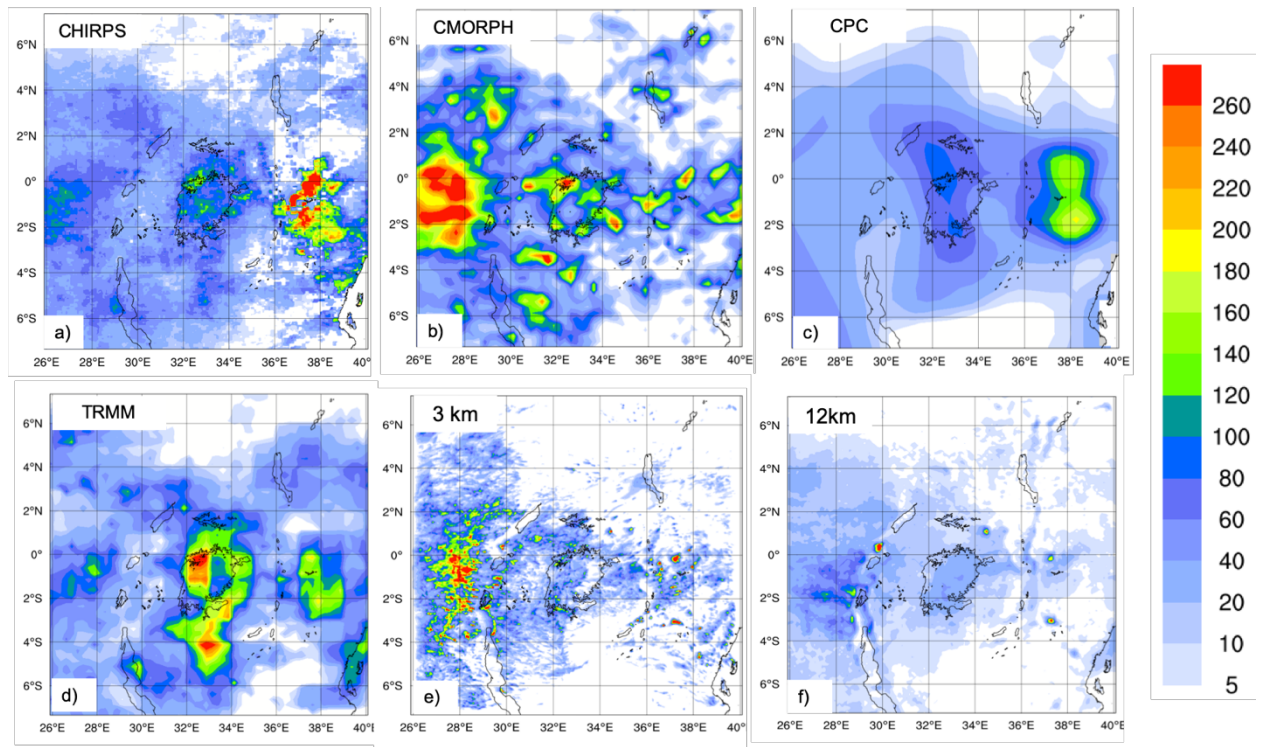
602



603

604 **Figure 10 : Longitude-time (hourly) Hovmöller diagram of LKV domain surface temperature**
 605 **anomaly (shading, in K). Panels correspond to the 3km simulation (left) and 12km**
 606 **simulation (right). The lake Victoria is between 32°E and 34°E longitude**

607



608

609 **Figure 11: Total event accumulated precipitation (mm) during the LKV case (November 25,**
 610 **1999-December 1, 1999) measured by CHIRPS (a), CMORPH (b), CPC (d) TRMM (e) and**
 611 **calculated by RegCM4 at 3 km (e) and 12 km (f).**

612

613 Figure 11 reports the total accumulated precipitation observed and simulated for the LKV
 614 case. TRMM (Figure 11d) and CPC (Figure 11c) show a similar pattern, with two-rainfall
 615 maxima of different intensities over the southeastern and northwestern lake areas.
 616 CMORPH (Figure 11b) shows a western rainfall maximum similar to TRMM and one large
 617 rainfall area almost entirely centered over the highlands to the west of the lake.
 618 Conversely in CHIRPS (Figure 11a) a maximum is found to the east of the lake while
 619 several localized maxima occur over the lake. The differences among the observed
 620 datasets highlight the issue of observational uncertainty and the need to take into
 621 consideration shortcomings associated with the types of observational datasets
 622 considered. Different datasets can have significantly different climatologies, especially in
 623 areas of low data availability. For example, Prein and Gobiet (2017) analyzed two gauge-
 624 based European-wide datasets, and seven global low-resolution datasets, and found

625 large differences across the observation products, often of similar magnitude as the
626 difference among model simulations. In this case and for this area the observation
627 uncertainty plays a big role especially at high resolution, and highlights the need for an
628 adequate observational network for model validation. However, despite the large
629 uncertainty among the different observed datasets (Figure 11 a-d), we find a significant
630 underestimation of the precipitation by the 12 km run over the lake independently of the
631 dataset used as a reference (Figure 11f). In contrast, the 3 km simulation (Figure 11e)
632 shows substantially greater detail, with rainfall patterns more in agreement with the
633 CMORPH data. In particular, the 3 km simulation reproduces well the local rainfall
634 maxima on the western side of the lake, although these appear more localized and with
635 a multi-cell structure compared to CMORPH and TRMM. Additionally, the 12 km
636 simulation underestimates the observed heavy rainfall totals in the highlands to the west
637 of the lake region especially when compared to CMORPH, which are instead reproduced
638 by the 3 km simulation.

639 This last test case demonstrates the ability of RegCM4-NH in simulating realistic
640 convective activity over a such morphologically complex region, which is a significant
641 improvement compared to the hydrostatic-coarse resolution model configuration.

642

643 **Conclusions and future outlook**

644

645 In this paper we have described the development of RegCM4-NH, a non hydrostatic
646 version of the regional model system RegCM4, which was completed in response to the
647 need of moving to simulations at convection-permitting resolutions of a few kilometers.
648 The non-hydrostatic dynamical core of MM5 has been incorporated into the RegCM4
649 system previously based on the MM5 hydrostatic core. Some modifications to the MM5
650 dynamical core were also implemented to increase the model stability for long term runs.
651 RegCM4-NH also includes two explicit cloud microphysics schemes needed to explicitly
652 describe convection and cloud processes in the absence of the use of cumulus
653 convection schemes. Finally, we presented a few case studies of explosive convection to

654 illustrate how the model provides realistic results in different settings and general
655 improvements compared to the coarser resolution hydrostatic version of RegCM4 for
656 such types of events.

657
658 As already mentioned, RegCM4-NH is currently being used for different projects, and
659 within these contexts, is being run at grid spacings of a few kilometers for continuous
660 decadal simulations, driven by reanalyses of observations or GCM boundary conditions
661 (with the use of an intermediate resolution domains) over different regions, such as the
662 Alps, the Eastern Mediterranean, Central-Eastern Europe and the Caribbeans. These
663 projects, involving multi-model inter-comparisons, indicate that the performance of
664 RegCM4-NH is generally in line with that of other convection-permitting models, and
665 exhibits similar improvements compared to coarser resolution models, such as a better
666 simulation of the precipitation diurnal cycle and of extremes at hourly to daily time scales.
667 The results obtained within the multi-model context confirm previous results from single-
668 model studies (Kendon et al. 2012, 2017, Ban et al. 2014, 2015; Prein et al. 2015, 2017),
669 but also strengthen the robustness of the findings through reduced uncertainty compared
670 to coarse resolution counterpart (Ban et al., 2021, Pichelli et al., 2021). The convection-
671 permitting scale can thus open the perspective of more robust projections of future
672 changes of precipitation, especially over sub-daily time scales.

673
674 One of the problems of the RegCM4-NH dynamical core is that, especially for long runs
675 with varied meteorological conditions, a relatively short time step is needed for stability
676 reasons. This makes the model rather computationally demanding, although not more
677 than other convection-permitting modeling systems such as the Weather Research and
678 Forecast model (WRF, Skamarok et al. 2008). For this reason, we are currently
679 incorporating within the RegCM system a very different and more computationally efficient
680 non-hydrostatic dynamical core, which will provide the basis for the next version of the
681 model, RegCM5, to be released in the future.

682
683 Following the philosophy of the RegCM modeling system, RegCM4-NH is intended to be
684 a public, free, open source community resource for external model users. The non-

685 hydrostatic dynamical core has been implemented in a way that it can be activated in
686 place of the hydrostatic dynamics through a user-set switch, which makes the use of
687 RegCM4-NH particularly simple and flexible. We therefore envision that the model will be
688 increasingly used by a broad community so that a better understanding can be achieved
689 of its behavior, advantages and limitations.

690

691 **Code availability:** <https://zenodo.org/record/4603556>

692 **Cases study configuration files:** <https://zenodo.org/record/5106399>

693

694

695 **Author contribution:** CE prepared the manuscript with contributions from all co-authors
696 and coordinated research, SP, TA, GR carried out and analysed the simulations, PE
697 investigated solutions to stabilize/adapt the model at the km-scale and performed
698 preliminary validation tests, GG developed/adapted the model code, FDS contributed to
699 develop the coupled version of the model, NR developed one of the microphysics
700 scheme, GF supervised and coordinated all activities.

701

702 **Competing interests:** The authors declare that they have no conflict of interest.

703

704

705 **References**

706 Anthes, R. A., Hsie, E. -Y., and Kuo, Y. -H.: Description of the Penn State/NCAR
707 Mesoscale Model: Version 4 (MM4) (No. NCAR/TN-282+STR), doi:10.5065/D64B2Z90,
708 1987.

709 Anyah R.O. and Semazzi F.: Idealized simulation of hydrodynamic characteristics of Lake
710 Victoria that potentially modulate regional climate, *Int. J. Climatol.* 29(7):971–981.
711 doi:[10.1002/joc.1795](https://doi.org/10.1002/joc.1795), 2009.

712 Anyah, R., Semazzi, F. H. M. and Xie, L.: Simulated Physical Mechanisms Associated
713 with Climate Variability over Lake Victoria Basin in East Africa, *Mon. Wea. Rev.*, 134
714 3588-3609, 2006.

715 Ashouri, H., Hsu, K., Sorooshian, S., Braithwaite, D. K., Knapp, K. R., Cecil, L. D., Nelson,
716 B. R. and Prat, O. P.: PERSIANN-CDR: Daily Precipitation Climate Data Record from
717 Multisatellite Observations for Hydrological and Climate Studies, *Bulletin of the American*
718 *Meteorological Society*, 96(1), 69-83, doi : 10.1175/BAMS-D-13-00068.1, 2015.
719

720 Ban, N., Schmidli, J., and Schär ,C.: Evaluation of the convection-resolving regional
721 climate modeling approach in decade-long simulations, *J. Geophys. Res. Atmos.*, 119,
722 7889– 7907, <https://doi.org/10.1002/2014JD021478>, 2014.
723

724 Ban, N., Schmidli, J., and Schär ,C.: Heavy precipitation in a changing climate: does short-
725 term summer precipitation increase faster?, *Geophys Res Lett* 42:1165–1172.
726 <https://doi.org/10.1002/2014GL062588>, 2015
727

728 Ban, N., Caillaud, C., Coppola, E. et al.: The first multi-model ensemble of regional climate
729 simulations at kilometer-scale resolution, part I: evaluation of precipitation, *Clim Dyn* .
730 <https://doi.org/10.1007/s00382-021-05708-w>, 2021.
731

732 Beheng, K.: A parameterization of warm cloud microphysical conversion processes,
733 *Atmos. Res.*, 33, 193–206, 1994
734

735 Bennington, V., Notaro, M. and Holman, K.D.: Improving Climate Sensitivity of Deep
736 Lakes within a Regional Climate Model and Its Impact on Simulated Climate, *J. Climi*, 27,
737 2886-2911, 2014.
738

739 Bretherton, C.S., McCaa, J.R., and Grenier, H.: A new parameterization for shallow
740 cumulus convection and its application to marine subtropical cloud-topped boundary lay-
741 ers. I. Description and 1D results, *Mon Weather Rev* 132: 864– 882, 2004.
742

743 Chan, S. C., Kendon, E. J., Fowler, H. J., Blenkinsop, S., Roberts, N. M. and Ferro,
744 C.A.T.: The value of high- resolution Met Office regional climate models in the simulation

745 of multi-hourly precipitation extremes, *J. Climate*, 27, 6155–6174,
746 <https://doi.org/10.1175/JCLI-D-13-00723.1>, 2014.

747
748 Chen, M. and Xie, P.: CPC Unified Gauge-based Analysis of Global Daily Precipitation,
749 *2008 Western Pacific Geophysics Meeting*. ISBN: 0026- 0576. DOI:
750 [http://dx.doi.org/10.1016/S0026-0576\(07\)80022-5](http://dx.doi.org/10.1016/S0026-0576(07)80022-5), 2008.

751
752 Clark, P., Roberts, N., Lean, H. , Ballard, S. P. and Charlton- Perez, C.: Convection-
753 permitting models: A step-change in rainfall forecasting, *Meteor. Appl.*, 23, 165–181,
754 <https://doi.org/10.1002/met.1538>, 2016.

755
756 Coppola, E., Sobolowski, S., Pichelli, E. et al. A first-of-its-kind multi-model convection
757 permitting ensemble for investigating convective phenomena over Europe and the
758 Mediterranean. *Clim Dyn* 55, 3–34, <https://doi.org/10.1007/s00382-018-4521-8>, 2020.

759
760 Coppola, E., Giorgi, F., Mariotti, L. and Bi, X.: RegT-Band: a tropical band version of
761 RegCM4, *Clim Res* 52: 115–133, 2012.

762
763 Dacre, H. F., Clark, P. A., Martinez-Alvarado, O., Stringer, M. A. and Lavers, D. A.: How
764 do atmospheric rivers form?, *Bull. Amer. Meteor. Soc.*, 96, 1243-1255,
765 <https://doi.org/10.1175/BAMS-D-14-00031>, 2015.

766
767 Dale, M., Hosking, A., Gill, E., Kendon, E. J., Fowler, H. J., Blenkinsop, S. and Chan, S.
768 C.: Understanding how changing rainfall may impact on urban drainage systems; les-
769 sons from projects in the UK and USA, *Water Pract. Technol.*, 13, 654–661,
770 <https://doi.org/10.2166/wpt.2018.069>, 2018.

771
772 Diallo, I., Giorgi, F. and Stordal, F.: Influence of Lake Malawi on regional climate from a
773 double nested regional climate model experiment, *Climate Dynamics*, 50, 3397– 3411.
774 <https://doi.org/10.1007/s00382-017-3811-x>, 2018.

775

776 Dickinson, R.E., Errico, R.M., Giorgi, F. et al.: A regional climate model for the western
777 United States, *Climatic Change* 15, 383–422 (1989),
778 <https://doi.org/10.1007/BF00240465>, 2018.
779

780 Dickinson, R.E., Henderson-Sellers, A. and Kennedy, P.: Bio -sphere– atmosphere
781 transfer scheme (BATS) version 1eas coupled to the NCAR community climate model,
782 TechRep, National Center for Atmospheric Research TechNote NCAR.TN-387+ STR,
783 NCAR, Boulder, CO, 1993.
784

785 Done, J., Davis, C. A. and Weisman M. L.: The next gener- ation of NWP: Explicit
786 forecasts of convection using the Weather Research and Forecasting (WRF) model,
787 *Atmos. Sci. Lett.*, 5, 110–117, <https://doi.org/10.1002/asl.72>, 2004.
788

789 Dudhia, J.: Numerical study of convection observed during the winter monsoon
790 experiment using a mesoscale two-dimensional model, *J. Atmos. Sci.*, 46, 3077–3107,
791 1989.
792

793 Durran, D.R. and Klemp, J.B.: A compressible model for the simulation of moist mountain
794 waves, *Mon. Wea. Rev.*, 111, 2341–236, 1983.
795

796 Elguindi, N., Bi, X., Giorgi, F. , Nagarajan, B., Pal J., Solmon, F., Rauscher, S., Zakey,
797 S., O'Brien, T., Nogherotto, R. and Giuliani, G.: Regional Climate Model RegCM
798 Reference Manual Version 4.7, 49 pp, <https://zenodo.org/record/4603616>, 2017.
799

800 Emanuel, K.A.: A scheme for representing cumulus convection in large-scale models, *J.*
801 *Atmos. Sci.*, 48, 2313–2335, 1991.
802

803 Fairall, C.W., Bradley, E.F., Godfrey, J.S. , Wick, G.A., Edson, J.B. and Young, G.S.: The
804 cool skin and the warm layer in bulk flux calculations, *J. Geophys. Res.*, 101, 1295-1308,
805 1996a.
806

807 Fairall, C.W., Bradley, E.F., Rogers, D.P., Edson, J.B. and Young, G.S.: Bulk
808 parameterization of air-sea fluxes for TOGA COARE, *J. Geophys. Res.*, 101, 3747-3764,
809 1996b.

810

811 Funk, C., Peterson, P., Landsfeld, M. et al. The climate hazards infrared precipitation with
812 stations—a new environmental record for monitoring extremes, *Sci Data* 2, 150066,
813 <https://doi.org/10.1038/sdata.2015.66>, 2015.

814

815 Gimeno, L., Nieto, R., Vázquez, M. and Lavers, D. A.: Atmospheric rivers: A mini-review,
816 *Front. Earth Sci.*, 2, <https://doi.org/10.3389/feart.2014.00002>, 2014.

817

818 Giorgi F.: Thirty years of regional climate modeling: where are we and where are we going
819 next?, *J Geophys Res Atmos* 124:5696–5723, 2019.

820

821 Giorgi, F., Coppola, E., Solmon, F., Mariotti, L. et al.: RegCM4: model description and
822 preliminary tests over multiple CORDEX domains, *Clim Res* 52:7-29.
823 <https://doi.org/10.3354/cr01018>, 2012.

824

825 Giorgi, F., Francisco, R. and Pal, J.S.: Effects of a sub-gridscale topography and landuse
826 scheme on surface climate and hydrology. I. Effects of temperature and water vapor
827 disaggregation, *J Hydrometeorol.*, 4, 317– 333, 2003.

828

829 Giorgi, F., Jones, C. and Asrar, G.: Addressing climate information needs at the regional
830 level: the CORDEX framework, *WMO Bull*, 175–183, 2009.

831

832 Giorgi, F. and Mearns, L.O.: Introduction to special section: regional climate modeling
833 revisited, *J Geophys Res*, 104, 6335–6352, 1999.

834

835 Giorgi, F., Marinucci, M.R. and Bates, G.: Development of a second generation regional
836 climate model (RegCM2). I. Boundary layer and radiative transfer processes, *Mon*
837 *Weather Rev.*, 121, 2794–2813, 1993a.

838 Giorgi, F., Marinucci, M.R., Bates, G. and De Canio, G.: Development of a second
839 generation regional climate model (RegCM2), part II: convective processes and
840 assimilation of lateral boundary conditions, *Mon. Weather Rev.*, 121, 2814–2832, 1993b.
841

842 Giorgi, F., and Bates, G.T.: The Climatological Skill of a Regional Model over Complex
843 Terrain, *Mon. Wea. Rev.*, 117, 2325–2347, [https://doi.org/10.1175/1520-
844 0493\(1989\)117<2325:TCSOAR>2.0.CO;2](https://doi.org/10.1175/1520-0493(1989)117<2325:TCSOAR>2.0.CO;2), 1989.
845

846 Grell, G.A.: Prognostic evaluation of assumptions used by cumulus parameterizations,
847 *Mon. Weather Rev.* 121, 764– 787, 1993.
848

849 Grell, G.A., Dudhia J. and Stauffer, D. R.: A Description of the Fifth Generation Penn
850 State/NCAR Mesoscale Model (MM5), NCAR Tech. Note, NCAR/TN-398+ STR, Boulder,
851 p. 122, 1994.
852

853 Gunn, K. L. S., and Marshall, J. S. : The distribution with size of aggregate snowflakes, *J.*
854 *Meteor.*, 15, 452–461, [https://doi.org/10.1175/1520-
855 0469\(1958\)015<0452:TDWSOA>2.0.CO;2](https://doi.org/10.1175/1520-0469(1958)015<0452:TDWSOA>2.0.CO;2), 1958.
856

857 Gutowski Jr., W. J., Giorgi, F., Timbal, B., Frigon, A., Jacob, D., Kang, H.-S., Raghavan,
858 K., Lee, B., Lennard, C., Nikulin, G., O'Rourke, E., Rixen, M., Solman, S., Stephenson,
859 T., and Tangang, F.: WCRP COordinated Regional Downscaling EXperiment (CORDEX):
860 a diagnostic MIP for CMIP6, *Geosci. Model Dev.*, 9, 4087–4095,
861 <https://doi.org/10.5194/gmd-9-4087-2016>, 2016.
862

863 Holtslag, A., de Bruijn, E. and Pan, H.L.: A high resolution air mass transformation model
864 for short-range weather fore-casting, *Mon Weather Rev* 118: 1561–1575, 1990.
865

866 Hostetler, S.W., Bates, G.T. and Giorgi, F.: Interactive nesting of a lake thermal model
867 within a regional climate model for climate change studies, *J Geophys Res* 98: 5045–
868 5057, 1993.

869 Huffman, G. J., Bolvin, D. T., Nelkin, E. J., Wolff, D. B., Adler, R. F., Gu, G., Hong, Y.,
870 Bowman, K. P. and Stocker, E. F.: The TRMM Multisatellite Precipitation Analysis
871 (TMPA): Quasi-global, multiyear, combined-sensor precipitation estimates at fine scales,
872 *J. Hydrometeor.*, 8, 38–55, doi:<https://doi.org/10.1175/JHM560.1>, 2007.

873

874 Kiehl, J., Hack, J., Bonan, G., Boville, B., Breigleb, B., Williamson, D. and Rasch, P.:
875 Description of the NCAR Community Climate Model (CCM3), National Center for
876 Atmospheric Research Tech Note NCAR/TN-420+ STR, NCAR, Boulder, CO, 1996.

877

878 Lean, H. W., Clark, P. A., Dixon, M., Roberts, N. M., Fitch, A., Forbes, R. and Halliwell,
879 C.: Characteristics of high-resolution versions of the Met Office Unified Model for
880 forecasting convection over the United Kingdom, *Mon. Wea. Rev.*, 136, 3408–3424,
881 <https://doi.org/10.1175/2008MWR2332.1>, 2008.

882

883 Lind, P., Lindstedt, D., Kjellstrom, E. and Jones, C.: Spatial and temporal characteristics
884 of summer precipitation over central Europe in a suite of high-resolution climate models,
885 *J. Climate*, 29, 3501–3518, <https://doi.org/10.1175/JCLI-D-15-0463.1>, 2016.

886

887 Hewitt, C. D. and Lowe, J. A.: Toward a European climate prediction system, *Bull. Amer.*
888 *Meteor. Soc.*, 99, 1997–2001, <https://doi.org/10.1175/BAMS-D-18-0022.1>, 2018.

889

890 Hong, S.-Y., Juang, H.-M. H. and Zhao, Q.: Implementation of prognostic cloud scheme
891 for a regional spectral model, *Mon. Wea. Rev.*, 126, 2621–2639, 1998.

892

893 Hong, S.-Y., Dudhia, J. and Chen, S.-H.: A Revised Approach to Ice Microphysical
894 Processes for the Bulk Parameterization of Clouds and Precipitation, *Mon. Wea. Rev.*,
895 132, 103–120, 2004.

896

897 Hong, S.-Y., and Lim, J.-O. J.: The WRF Single-Moment 6-Class Microphysics Scheme
898 (WSM6), *J. Korean Meteor. Soc.*, 42, 129–151, 2006.

899

900 Hostetler, S.W., Bates, G.T. and Giorgi, F.: Interactive Coupling of Lake Thermal Model
901 with a Regional climate Model, *J. Geophys. Res.*, 98(D3), 5045-5057, 1993.
902

903 Huffman, G. J., Bolvin, D. T., Nelkin, E. J., Wolff, D. B., Adler, R. F., Gu, G., Hong, Y.,
904 Bowman, K. P. and Stocker, E. F.: The TRMM Multisatellite Precipitation Analysis
905 (TMPA): Quasi-Global, Multiyear, Combined-Sensor Precipitation Estimates at Fine
906 Scales, *Journal of Hydrometeor.*, 8(1), 38-55, DOI: 10.1175/JHM560.1, 2007.
907

908 Joyce, R. J., Janowiak, J. E., Arkin, P. A. and Xie, P.: CMORPH: A Method that Produces
909 Global Precipitation Estimates from Passive Microwave and Infrared Data at High Spatial
910 and Temporal Resolution. *J. Hydrometeor.*, 5(3), 487–503, 2004.
911

912 Kain, J. S.: The Kain–Fritsch convective parameterization: An update, *J. Appl. Meteor.*,
913 43, 170–181, [https://doi.org/10.1175/1520-0450\(2004\)043](https://doi.org/10.1175/1520-0450(2004)043<0170:TKCPAU>2.0.CO;2)
914 2004.
915

916 Kain, J. S. and Fritsch, J. M.: A one-dimensional entraining/ detraining plume model and
917 its application in convective parameterization, *J. Atmos. Sci.*, 47, 2784–2802, 1990.
918

919 Kendon, E. J., Roberts, N. M., Senior, C. A. and Roberts, M. J.: Realism of rainfall in a
920 very high-resolution regional climate model, *J. Climate*, 25, 5791–5806, [https://doi.org/](https://doi.org/10.1175/JCLI-D-11-00562.1)
921 10.1175/JCLI-D-11-00562.1, 2012.
922

923 Kendon, E. J., Ban, N., Roberts, N. M., Fowler, H. J., Roberts, M. J., Chan, S. C., Evans,
924 J. P., Fosser, G. and Wilkinson, J. M.: Do convection-permitting regional climate models
925 improve projections of future precipitation change?, *Bull. Amer. Meteor. Soc.*, 98, 79–93,
926 [https://doi.org/ 10.1175/BAMS-D-15-0004.1](https://doi.org/10.1175/BAMS-D-15-0004.1), 2017.
927

928 Kessler, E.: On the Distribution and Continuity of Water Substance in Atmospheric
929 Circulations, *Meteor. Monogr.*, No. 32, Amer. Meteor. Soc., 84 pp, 1969.
930

931 Khairoutdinov, M. and Kogan, Y.: A new cloud physics parameterization in a large-eddy
932 simulation model of marine stratocumulus, *Bull. Amer. Meteorol. Soc.*, 128, 229–243,
933 2000

934

935 Klemp, J.B. and Dudhia, J.: An Upper Gravity-Wave Absorbing Layer for NWP
936 Applications, *Monthly Weather Review*, 176, 3987-4004, 2008.

937

938 Klemp, J. B. and Lilly, D. K.: Numerical simulation of hydrostatic mountain waves, *J.*
939 *Atmos. Sci.*, 35, 78–107, 1978.

940

941 Lin, Y., Farley, R. and Orville, H.: Bulk parameterization of the snow field in a cloud model,
942 *J. Appl. Meteor. Clim.*, 22, 1065–1092, 1983.

943

944 Marshall, J. S. and Palmer, W. M. K.: The distribution of raindrops with size. *J. Meteor.*,
945 5, 165–166, 1948.

946

947 Matte, D., Laprise, R., Thériault, J. M. and Lucas-Picher, P.: Spatial spin-up of fine scales
948 in a regional climate model simulation driven by low-resolution boundary conditions.
949 *Climate Dynamics*, 49(1-2), 563–574. doi:10.1007/s00382-016-3358-2, 2017.

950

951 Mlawer, E. J., Taubman, S. J., Brown, P. D., Iacono, M. J. and Clough, S. A.: Radiative
952 transfer for inhomogeneous atmospheres: RRTM, a validated correlated-k model for the
953 longwave, *J. Geophys. Res.*, 102, 16663-16682, 1997.

954

955 Nogherotto, R., Tompkins, A.M., Giuliani, G., Coppola, E. and Giorgi, F.: Numerical
956 framework and performance of the new multiple-phase cloud microphysics scheme in
957 RegCM4. 5: precipitation, cloud microphysics, and cloud radiative effects. *Geoscientific*
958 *Model Development*, 9(7), 2533-2547, 2016.

959

960 Oleson, K. W., Lawrence, D. M., Bonan, G. B., Drewniak, B., Huang, M., Koven, C. D.,
961 Levis, S., Li, F., Riley, W. J., Subin, Z. M., Swenson, S. C., Thornton, P. E., Bozbiyik, A.,
962 Fisher, R., Kluzek, E., Lamarque, J. -F., Lawrence, P. J., Leung, L. R., Lipscomb, W.,
963 Muszala, S., Ricciuto, D. M., Sacks, W., Sun, Y., Tang, J., and Yang, Z. -L: Technical
964 Description of version 4.5 of the Community Land Model (CLM), Ncar Technical Note
965 NCAR/TN-503+STR, National Center for Atmospheric Research, Boulder, CO, 422 pp,
966 DOI: 10.5065/D6RR1W7M, 2013.

967
968 Pal, J.S., Small, E. and Eltahir, E.: Simulation of regional-scale water and energy
969 budgets: representation of subgrid cloud and precipitation processes within RegCM, J
970 Geo-phys Res 105: 29579–29594, 2000.

971
972 Pal, J. S., Giorgi, F., Bi, X., Elguindi, N., Solmon, F., Gao, X., Rauscher, S. A., Francisco,
973 R., Zakey, A., Winter, J., Ashfaq, M., Syed, F. S., Bell, J. L., Diffenbaugh, N. S.,
974 Karmacharya, J., Konaré, A., Martinez, D., da Rocha, R. P., Sloan, L. C. and Steiner, A.
975 L.: The ICTP RegCM3 and RegCNET: regional climate modeling for the developing world.
976 Bull. Amer. Meteorol. Soc., 88(9), 1395–1409, 2007.

977
978 Pichelli, E., Coppola, E., Sobolowski, S. et al.: The first multi-model ensemble of regional
979 climate simulations at kilometer-scale resolution part 2: historical and future simulations
980 of precipitation, Clim. Dyn., <https://doi.org/10.1007/s00382-021-05657-4>, 2021.

981
982 Prein, A. F. and Gobiet, A.: Impacts of uncertainties in European gridded precipitation
983 observations on regional climate analysis, International Journal of Climatology. ISSN:
984 10970088. DOI: 10.1002/joc.4706, 2017.

985
986 Prein, A. F., Langhans, W., Fosser, G., Ferrone, A., Ban, N., Goergen, K., Keller, M.,
987 Tölle, M., Gutjahr, O., Feser, F., et al.: A review on regional convection-permitting climate
988 modeling: demonstrations, prospects, and challenges, Rev. Geophys. 53, 323–361,
989 2015.

990

991 Ralph, F. M., Neiman, P. J., Wick, G. A., Gutman, S. I., Dettinger, M. D., Cayan, D. R.
992 and White, A. B.: Flooding on California's Russian River: Role of atmospheric rivers,
993 *Geophys. Res. Lett.*, 33, L13801, <https://doi.org/10.1029/2006GL026689>, 2006.
994

995 Ralph, F. M., Dettinger, M. D., Cairns, M. M., Galarneau, T. J. and Eylander, J.: Defining
996 "atmospheric river": How the Glossary of Meteorology helped resolve a debate. *Bull.*
997 *Amer. Meteor. Soc.*, 99, 837–839, <https://doi.org/10.1175/BAMS-D-17-0157.1>, 2018.
998

999 Rutledge, S. A. and Hobbs, P. V.: The mesoscale and microscale structure and
1000 organization of clouds and precipitation in midlatitude cyclones. Part VIII: A model for the
1001 "seeder-feeder" process in warm-frontal rainbands, *J. Atmos. Sci.*, 40, 1185–1206, 1983.
1002

1003 Skamarock, W.C., Klemp, J.B., Dudhia, J., Gill, D.O., Barker, D.M., Duda, M.G., Huang,
1004 X.Y., Wang, W. and Powers, J.G.: A description of the advanced research WRF version
1005 3, Technical Note NCAR/TN-475+STR. NCAR: Boulder, CO, 2008.
1006

1007 Schwartz, C. S.: Reproducing the September 2013 record- breaking rainfall over the
1008 Colorado Front Range with high- resolution WRF forecasts, *Wea. Forecasting*, 29, 393–
1009 402, <https://doi.org/10.1175/WAF-D-13-00136.1>, 2014.
1010

1011 Sitz, L. E., Sante, F., Farneti, R., Fuentes-Franco, R., Coppola, E., Mariotti, L., Reale, M.
1012 et al.: Description and Evaluation of the Earth System Regional Climate Model (RegCM–
1013 ES), *Journal of Advances in Modeling Earth Systems*. doi:10.1002/2017MS000933,
1014 2017.
1015

1016 Song, Y., Semazzi, H.M.F., Xie, L. and Ogallo, L.J.: A coupled regional climate model for
1017 the Lake Victoria Basin of East Africa, *Int. J. Climatol.* 24: 57-75, 2004.
1018

1019 Sun, X., Xie, L., Semazzi, F. and Liu, B.: Effect of Lake Surface Temperature on the
1020 Spatial Distribution and Intensity of the Precipitation over the Lake Victoria Basin, *Mon.*
1021 *Wea. Rev.* 143: 1179-1192, 2015.

1022
1023 Sundqvist, H., Berge, E. and Kristjansson, J.: Condensation and cloud parameterization
1024 studies with a mesoscale numerical weather prediction model, Mon. Weather Rev., 117,
1025 1641–1657, 1989.
1026
1027 Talling, J. F.: The incidence of vertical mixing, and some biological and chemical
1028 consequences, in tropical African lakes, Verh. Int. Ver. Limnol. 17, 998-1012 DOI:
1029 10.1080/03680770.1968.11895946, 1969.
1030
1031 Tiedtke, M.: A comprehensive mass flux scheme for cumulus parametrization in large-
1032 scale models, Mon. Weather Rev., 117, 1779–1800, 1989.
1033
1034 Tiedtke, M.: Representation of Clouds in Large-Scale Models, Mon. Wea. Rev., 121,
1035 3040–3061, [https://doi.org/10.1175/1520-0493\(1993\)121](https://doi.org/10.1175/1520-0493(1993)121<3040:ROCILS>2.0.CO;2)<3040:ROCILS>2.0.CO;2,
1036 1993.
1037
1038 Tiedtke, M.: An extension of cloud-radiation parameterization in the ECMWF model: The
1039 representation of subgrid-scale variations of optical depth, Mon. Wea. Rev., 124, 745–
1040 750, 1996.
1041
1042 Tompkins, A.: Ice supersaturation in the ECMWF integrated forecast system, Q. J. Roy.
1043 Meteor. Soc., 133, 53–63, 2007
1044
1045 Tripoli, G. J., and W. R. Cotton: A numerical investigation of several factors contributing
1046 to the observed variable intensity of deep convection over south Florida, J. Appl. Meteor.,
1047 19, 1037–1063, 1980.
1048
1049 Williams, P.D.: A proposed modification to the Robert–Asselin time filter, Mon. Weather
1050 Rev. 137: 2538–2546, 2009.
1051

1052 Weisman, M. L., Davis, C., Wang, W., Manning, K. W. and Klemp, J. B.: Experiences
1053 with 0–36-h explicit convective forecasts with the WRF-ARW model, *Wea. Forecasting*,
1054 23, 407–437, <https://doi.org/10.1175/2007WAF2007005.1>, 2008.

1055
1056 Weusthoff, T., Ament, F., Arpagaus, M. and Rotach, M. W.: Assessing the benefits of
1057 convection-permitting models by neighborhood verification: Examples from MAP D-
1058 PHASE, *Mon. Wea. Rev.*, 138, 3418–3433, <https://doi.org/10.1175/2010MWR3380.1>,
1059 2010.

1060
1061 Zeng, X., Zhao, M. and Dickinson, R.E.: Intercomparison of bulk aerodynamic algorithms
1062 for the computation of sea surface fluxes using TOGA COARE and TAO data, *J Clim* 11:
1063 2628–2644, 1998.

1064
1065 Zhu, Y., and Newell, R. E.: A proposed algorithm for moisture fluxes from atmospheric
1066 rivers, *Mon. Wea. Rev.*, 126, 725–735, [https://doi.org/10.1175/1520-](https://doi.org/10.1175/1520-0493(1998)126<0725:APAFMF>2.0.CO;2)
1067 0493(1998)126<0725:APAFMF>2.0.CO;2, 1998